Commun. Comput. Phys.
doi: 10.4208/cicp.OA-2024-0262

Vol. **39**, No. 5, pp. 1421-1453
May 2026

A Lagrangian GRP Algorithm for Axisymmetric Problems of Compressible Fluids

Zijin Zhu[1], Min Xiao[2], Jiwei Zhang[1] and Guoxi Ni[3,*]

[1] *School of Mathematics and Statistics, Wuhan University, Wuhan, China.*
[2] *College of Science, China University of Petroleum, Beijing, China.*
[3] *Institute of Applied Physics and Computational Mathematics, Beijing, China.*

Communicated by Kun Xu

Received 29 October 2024; Accepted (in revised version) 23 March 2025

Abstract. We devise a Lagrangian Generalized Riemann Problem (GRP) algorithm for axisymmetric hydrodynamics, which pays attention to high-resolution boundary treatment at the symmetric axis. The numerical boundary condition here is first formulated the same as the scheme on interior cells. Then we uniformly obtain the requisite interface values in constructing numerical fluxes and sources through the newly-tailored GRP solver and its one-sided variant. There also exist some innovations in the other two critical procedures: the derivation of vertex velocities and the compliance with the geometry conservation law (GCL). Several challenging numerical examples are utilized to demonstrate the performance of our algorithm in resolving discontinuities, maintaining symmetry, alleviating overheating phenomena, and dealing with complex fluids.

AMS subject classifications: 76M12, 35L65, 65M08, 76N15

Key words: Axisymmetry, cell-centered Lagrangian algorithm, high-resolution numerical boundary condition, GRP solver, excess heating.

1 Introduction

The numerical simulations of axisymmetric multi-material flows play a vital role in numerous engineering applications, such as inertial confinement fusion, astrophysics, and weaponry equipment [8, 12, 36]. The dimensionality reduction induced by axisymmetry offers a signal computational advantage. And the Lagrangian algorithms are famous for

*Corresponding author. *Email addresses:* zhuzijin@whu.edu.cn (Z. Zhu), xiaomin@cup.edu.cn (M. Xiao), jiweizhang@whu.edu.cn (J. Zhang), gxni@iapcm.ac.cn (G. Ni)

the effective capture of material interfaces. However, except for the resolution of discontinuities, there still persist three tasks to confront in their collocation: the accordance with conservation law [34], the maintenance of spherical symmetry [10], and the appropriate boundary treatment at the symmetric axis $r=0$ [24]. Overcoming these intertwined issues unavoidably involves multiple trade-offs.

The axisymmetric schemes can fall into two main categories concerning the discrete manners: area-weighted and volume-weighted [22]. Each has its own pros and cons. The former only conserves mass. In contrast, the latter, primarily combined with the cell-centered style, can strictly conserve mass, momentum, and total energy [11]. As for the preservation of spherical symmetry on the polar mesh, the latter is much inferior [30].

The singularity of geometrical source at the inner boundary $r=0$ is another inescapable difficulty. We cannot totally predict its function in the absence of mathematical theories, especially when a reflected shock is formed. Well, that is exactly the most essential and anticipated part. Previous efforts on this issue include the extrapolation of neighboring solution [37], the import of heat viscosity [24], and so on. The straightforward use of reflective boundary condition is most common among them [9, 10, 20, 32]. Whereas, the research in [19] suggests its actual ignorance of source effect. Excess heating, numerical instabilities, and even non-physical solution can thus be produced.

Upon these investigations, we embark on the choice of a discrete manner, since the numerical solution at $r=0$ relies on it likewise [31]. A volume-weighted scheme on the flexible quadrilateral mesh is precisely the one we tend to adopt. Conceivably, the relevant algorithm will have strengths in ensuring the conservation and weaknesses in preserving the spherical symmetry. We hope that the latter can be improved under the applicable numerical boundary.

Our scheme is established through a geometrically compatible analysis under the finite volume framework, which reminds us that the numerical boundary condition at $r=0$ can take the same form. Its consistency with the conservation law is thus guaranteed. Then we proceed to the numerical approximations of the fluxes and sources at the interior interfaces and $r=0$. A feasible option comes from the Generalized Riemann Problem (GRP) solver and its one-sided version.

The studies on the GRP series could date back to [3] and have been widely exploited since then [4, 6, 14, 27, 36]. This type of solver can serve as a high-order extension of the associated Riemann problem solver and brings us two major benefits. Firstly, we can skip the operator splitting and naturally exhibit the source effect via the Lax-Wendroff approach [5, 18]. Secondly, we notice that the radial velocity vanishes at $r=0$ due to the symmetry argument. The one-sided GRP solver can utilize this to precisely describe the fluids here. With the experience on the Eulerian algorithms [38, 39], we believe that it can also make a difference in the Lagrangian ones, particularly in preserving the spherical symmetry and reducing the heating error.

Turning to the Lagrangian velocities, the linearized GRP solver has once been directly applied at vertices in [23], since the fluid structure with initial four regions is too complicated to be distinguished. In contrast, we opt to propose an entire version at interfaces

to leverage its advantage in capturing strong discontinuities. Meanwhile, there comes another challenge, deriving vertex velocities from interface normal ones.

The well-known CAVEAT algorithm incorporates a five-point least-squares method to complete the shift [1], which just attains first-order accuracy. Its second-order upgrade stems from a larger thirteen-point stencil [29]. Later, an adaptive hybrid edition of these two is put forth in [26], which encompasses a parameter to be tuned for each individual test. We hold the opinion that the calculation errors of vertex velocities are most likely born out of the discontinuous fields. By autonomously retaining the smoother parts, the thirteen-point stencil can be cut down to a narrower nine-point one. Our strategy aims to reduce computational errors and costs at the expense of some setup. Furthermore, the uneven distribution of points can conduce to the recovery of flow direction.

After the least-squares step, we are stuck in the dilemma of inconsistency between vertex velocities and face normal ones, which may cause spurious mesh motion. A plausible Lagrangian algorithm should meet the axisymmetric geometry conservation law (GCL). Thence we take it as a criterion and simply modify the face normal velocities reciprocally.

In summary, the contribution of our algorithm rests in the high-resolution numerical scheme and boundary condition. On execution, they are made possible by the newly developed GRP solver and the corresponding one-sided version. Under cell-centered discretization, we also hammer out a nine-point least-squares method and axisymmetric GCL modification for the Lagrangian computing mesh.

The remainder of this paper is organized as follows. In Section 2, we give the identical forms of our scheme and inner boundary condition at $r=0$. Our axisymmetric GRP solvers are introduced in Section 3. The nine-point least-squares method and axisymmetric GCL correction are unveiled in Section 4. We summarize the whole algorithm in Section 5 and present the numerical results in Section 6. The concluding remarks are made in Section 7. To facilitate programming, we collect some useful coefficients of the solver in Appendix.

2 The Lagrangian scheme for axisymmetric problems

We start with revisiting some fundamental facts about axisymmetric fluids. They will subsequently be incorporated in our cell-centered Lagrangian GRP scheme.

2.1 Fluid model

Imagine that a control volume $\Omega(t)$, surrounded by a piece-wise smooth boundary, moves with the fluid. Under the Lagrangian description, the integral form of the Eu-

ler equations on the volume $\Omega(t)$ reads

$$\begin{aligned}
&\frac{\mathrm{d}}{\mathrm{d}t}\iiint_{\Omega(t)}\rho \mathrm{d}V=0,\\
&\frac{\mathrm{d}}{\mathrm{d}t}\iiint_{\Omega(t)}\rho \boldsymbol{u}\mathrm{d}V=-\iint_{\partial\Omega(t)}p\boldsymbol{n}\mathrm{d}S,\\
&\frac{\mathrm{d}}{\mathrm{d}t}\iiint_{\Omega(t)}\rho E\mathrm{d}V=-\iint_{\partial\Omega(t)}p\boldsymbol{u}\cdot\boldsymbol{n}\mathrm{d}S,
\end{aligned} \tag{2.1}$$

where $\boldsymbol{n}$ is the outward unit vector normal to the boundary surface $\partial\Omega(t)$. The notations ρ, $\boldsymbol{u}$, p, and E represent the density, the velocity, the pressure, and the specific total energy in order. The system (2.1) can be closed by such a caloric equation of state (EOS),

$$p=p(\rho,e),$$

in which e is the specific internal energy. It connects with E via the relation $e=E-|\boldsymbol{u}|^2/2$.

In the cylindrical coordinates (r,θ,z), the volume element is written as $\mathrm{d}V=r\mathrm{d}r\mathrm{d}\theta\mathrm{d}z$, $r\geqslant 0$. Further for axisymmetric fluids, the flow variables are independent of the azimuthal direction θ, that is

$$[\rho,\boldsymbol{u},E]=[\rho,\boldsymbol{u},E](r,z,t).$$

Other than that, the azimuthal velocity vanishes. Designate u and v as the radial (r) and axial (z) velocity components, then the system (2.1) can be specified as

$$\begin{aligned}
&\frac{\mathrm{d}}{\mathrm{d}t}\iiint_{\Omega(t)}r\rho \mathrm{d}r\mathrm{d}\theta\mathrm{d}z=0,\\
&\frac{\mathrm{d}}{\mathrm{d}t}\iiint_{\Omega(t)}r\rho u\mathrm{d}r\mathrm{d}\theta\mathrm{d}z=-\iint_{\partial\Omega(t)}pn_r\mathrm{d}S+\iiint_{\Omega(t)}p\mathrm{d}r\mathrm{d}\theta\mathrm{d}z,\\
&\frac{\mathrm{d}}{\mathrm{d}t}\iiint_{\Omega(t)}r\rho v\mathrm{d}r\mathrm{d}\theta\mathrm{d}z=-\iint_{\partial\Omega(t)}pn_z\mathrm{d}S,\\
&\frac{\mathrm{d}}{\mathrm{d}t}\iiint_{\Omega(t)}r\rho E\mathrm{d}r\mathrm{d}\theta\mathrm{d}z=-\iint_{\partial\Omega(t)}p\tilde{u}\mathrm{d}S,
\end{aligned} \tag{2.2}$$

with the normal vector $\boldsymbol{n}=(n_r,n_z)$ and velocity $\tilde{u}=\boldsymbol{u}\cdot\boldsymbol{n}$ in terms of the boundary $\partial\Omega(t)$.

Remark 2.1. Based on Reynolds' transport theorem and Gauss' divergence theorem, we can derive an Eulerian description of axisymmetric fluids from the Lagrangian one (2.2):

$$\begin{aligned}
&\frac{\partial \boldsymbol{U}}{\partial t}+\frac{1}{r}\frac{\partial\big(r\boldsymbol{R}(\boldsymbol{U})\big)}{\partial r}+\frac{\partial \boldsymbol{Z}(\boldsymbol{U})}{\partial z}=\frac{\boldsymbol{\Phi}(\boldsymbol{U})}{r},\\
&\boldsymbol{U}=\begin{bmatrix}\rho\\ \rho u\\ \rho v\\ \rho E\end{bmatrix},\quad \boldsymbol{R}=\begin{bmatrix}\rho u\\ \rho u^2+p\\ \rho uv\\ u(\rho E+p)\end{bmatrix},\quad \boldsymbol{Z}=\begin{bmatrix}\rho v\\ \rho uv\\ \rho v^2+p\\ v(\rho E+p)\end{bmatrix},\quad \boldsymbol{\Phi}=\begin{bmatrix}0\\ p\\ 0\\ 0\end{bmatrix}.
\end{aligned} \tag{2.3}$$

In this study, the fluids are characterized by the polytropic gas EOS,

$$p=(\gamma-1)\rho e,\ \ \gamma>1, \tag{2.4}$$

where γ is the adiabatic exponent. The sound speed c thereof has the expression:

$$c=\sqrt{\frac{p}{\rho^2}\frac{\partial p}{\partial e}+\frac{\partial p}{\partial \rho}}=\sqrt{\frac{\gamma p}{\rho}}.$$

Substitution of the above two equations into the system (2.3) gives its alternative,

$$\begin{aligned}&\frac{\partial \boldsymbol{V}}{\partial t}+\boldsymbol{G}(\boldsymbol{V})\frac{\partial \boldsymbol{V}}{\partial r}+\boldsymbol{H}(\boldsymbol{V})\frac{\partial \boldsymbol{V}}{\partial z}=\boldsymbol{\Psi}(r,\boldsymbol{V}),\\ &\boldsymbol{V}=\begin{bmatrix}\rho\\ u\\ v\\ p\end{bmatrix},\quad \boldsymbol{G}=\begin{bmatrix}u & \rho & 0 & 0\\ 0 & u & 0 & 1/\rho\\ 0 & 0 & u & 0\\ 0 & \rho c^2 & 0 & u\end{bmatrix},\quad \boldsymbol{H}=\begin{bmatrix}v & 0 & \rho & 0\\ 0 & v & 0 & 0\\ 0 & 0 & v & 1/\rho\\ 0 & 0 & \rho c^2 & v\end{bmatrix},\quad \boldsymbol{\Psi}=-\frac{1}{r}\begin{bmatrix}\rho u\\ 0\\ 0\\ \rho c^2 u\end{bmatrix}.\end{aligned} \tag{2.5}$$

Denote the symbols $\mathbb{Z}$, $\mathbb{N}$, and $\mathbb{N}^+$ as the sets of whole integers, natural numbers, and positive integers. From the perspective of the (r,z)-plane, we split the computational domain, stretching to the symmetric axis $r=0$, into several non-overlapping quadrilateral cells $\mathcal{K}_{i,j}(t)$, $i\in\mathbb{N}$, $j\in\mathbb{Z}$. Here the subscripts i and j indicate the indexes of $\mathcal{K}_{i,j}(t)$ in the r and z directions respectively. The inner boundary cells at $r=0$ are $\mathcal{K}_{0,j}(t)$.

From a broader three-dimensional (3D) perspective, the real cell $\Omega_{i,j}(t)$ is generated by revolving $\mathcal{K}_{i,j}(t)$ around the axis $r=0$,

$$\Omega_{i,j}(t)=\big\{(r,\theta,z)\mid (r,z)\in\mathcal{K}_{i,j}(t),\ 0\leqslant\theta\leqslant 2\pi\big\}.$$

We explain these two perspectives in Fig. 1. An exceptional scenario is added within Fig. 1(c): The 3D cell $\Omega_{i,j}$ becomes cylindrical when its 2D counterpart $\mathcal{K}_{i,j}$ is rectangular. Setting $\boldsymbol{x}=(r,z)$, we sequentially label the centroid and four vertexes of $\mathcal{K}_{i,j}$ as $\boldsymbol{x}_{i,j}$, $\boldsymbol{x}_{i-1/2,j-1/2}$, $\boldsymbol{x}_{i+1/2,j-1/2}$, $\boldsymbol{x}_{i+1/2,j+1/2}$, and $\boldsymbol{x}_{i-1/2,j+1/2}$, see Fig. 1(a).

As shown in Fig. 1(b), the 3D cell $\Omega_{i,j}$ is mostly an irregular geometry. Given its similarities to frustums, we can write out its volume and area of each surface. Presume that the 2D cell $\mathcal{K}_{i,j}$ is non-concave (Fig. 2). Number its four edges counter-clock-wise as L_k ($k=1,2,3,4$), the vertices of which are $\boldsymbol{x}_k$ and $\boldsymbol{x}_{k+1}$ (let $\boldsymbol{x}_5=\boldsymbol{x}_1$). The volume of $\Omega_{i,j}$ is

$$|\Omega_{i,j}|=\iiint r\mathrm{d}r\mathrm{d}\theta\mathrm{d}z=\frac{\pi}{3}\sum_{k=1}^{4}(r_{k+1}^2+r_{k+1}r_k+r_k^2)\cdot(z_{k+1}-z_k). \tag{2.6}$$

The area of the surface $\mathcal{S}_k$, formed by rotating L_k around $r=0$, is

$$|\mathcal{S}_k|=\pi(r_{k+1}+r_k)\cdot|\boldsymbol{x}_{k+1}-\boldsymbol{x}_k|,\quad k=1,2,3,4. \tag{2.7}$$

It will hold for the boundary cells $\Omega_{0,j}$ ($j\in\mathbb{Z}$) likewise if we consider the area of their inner surfaces to be zero.

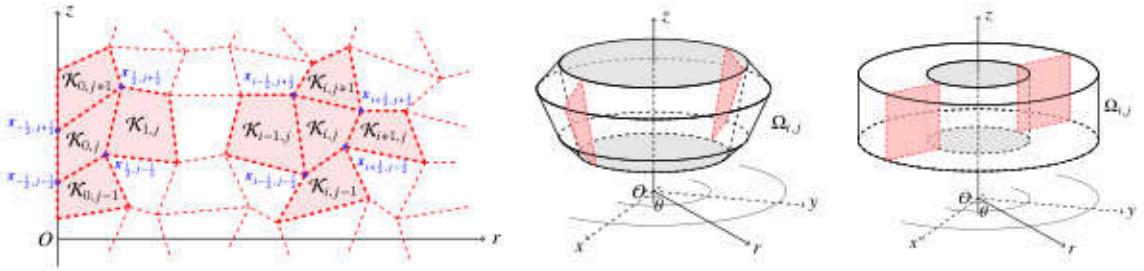

(a) $\mathcal{K}_{i,j}$. (b) $\Omega_{i,j}$. (c) Cylindrical $\Omega_{i,j}$.

Fig. 1: The computational cells under 2D and 3D views.

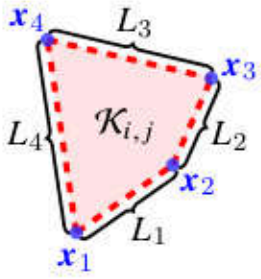

Fig. 2: The simplified notations about $\mathcal{K}_{i,j}$.

Remark 2.2. Using the symmetry argument, the radial velocity u at the axis $r=0$ satisfies

$$u(r=0,z,t)\equiv 0. \tag{2.8}$$

It means that if the computational domain contains $r=0$ from the start, the situation will remain unchanged. The boundary cells $\Omega_{0,j}(t)$ stay inseparable from it, $j\in\mathbb{Z}$. Noteworthily, the fluids there are quite complex. Excess heating often occurs in numerical calculations and requires careful processing [24]. We will discuss this in Section 3.2.

2.2 Fully Lagrangian discretization

On the basis of the foregoing preparation, let us devise a Lagrangian scheme, with second-order accuracy both in time and space, for axisymmetric fluids. Define the average of the conserved variable $r\boldsymbol{U}$ over the 3D cell $\Omega_{i,j}$ as

$$\overline{\boldsymbol{U}}_{i,j}(r,z,t)=\frac{1}{|\Omega_{i,j}|}\iiint_{\Omega_{i,j}} r\boldsymbol{U}(r,z,t)\mathrm{d}r\mathrm{d}\theta\mathrm{d}z$$

and the flux vector as $\boldsymbol{F}(\boldsymbol{U})=[0,pn_r,pn_z,p\widetilde{u}]^T$. The system (2.2) can be formulated as

$$\frac{\mathrm{d}}{\mathrm{d}t}\left(|\Omega_{i,j}|\overline{\boldsymbol{U}}_{i,j}\right)=-\iint_{\partial\Omega_{i,j}}\boldsymbol{F}(\boldsymbol{U})\mathrm{d}S+\iiint_{\Omega_{i,j}}\boldsymbol{\Phi}(\boldsymbol{U})\mathrm{d}r\mathrm{d}\theta\mathrm{d}z, \tag{2.9}$$

where the source term $\boldsymbol{\Phi}(\boldsymbol{U})$ and the cell volume $|\Omega_{i,j}|$ have been given in (2.3) and (2.6).

Next perform spatial discretization on the two integrals of (2.9). It suggests from Fig. 2 that a cell boundary $\partial\Omega_{i,j}$ consists of four surfaces. The surface integral can be approximated as

$$\iint_{\partial\Omega_{i,j}}\boldsymbol{F}(\boldsymbol{U})\mathrm{d}S=\sum_{k=1,2,3,4}\iint_{\mathcal{S}_k}\boldsymbol{F}(\boldsymbol{U})\mathrm{d}S\approx\sum_{k=1,2,3,4}\boldsymbol{F}_k|\mathcal{S}_k|,\quad \partial\Omega_{i,j}=\bigcup_{k=1,2,3,4}\mathcal{S}_k, \tag{2.10}$$

among which $\boldsymbol{F}_k:=\boldsymbol{F}(\boldsymbol{U}_k)$ is the numerical flux across the surface $\mathcal{S}_k$. These four variable values $\boldsymbol{U}_k$ ($k=1,2,3,4$) can be evaluated at each midpoint of L_k in the 2D view, precisely $\boldsymbol{U}_{i\pm1/2,j}:=\boldsymbol{U}\left(\boldsymbol{V}(r_{i\pm1/2},z_j,t)\right)$ and $\boldsymbol{U}_{i,j\pm1/2}:=\boldsymbol{U}\left(\boldsymbol{V}(r_i,z_{j\pm1/2},t)\right)$.

Later, we evaluate the volume integral of source term by the interface method [16],

$$\iiint_{\Omega_{i,j}}\boldsymbol{\Phi}(\boldsymbol{U})\mathrm{d}r\mathrm{d}\theta\mathrm{d}z=\iiint_{\Omega_{i,j}}\frac{\boldsymbol{\Phi}}{r}r\mathrm{d}r\mathrm{d}\theta\mathrm{d}z\approx\frac{|\Omega_{i,j}|}{r_{i,j}}\boldsymbol{\Sigma}_{i,j}, \tag{2.11}$$

where $\boldsymbol{\Sigma}_{i,j}$ is a weighted average of $\boldsymbol{\Phi}_k$ ($k=1,2,3,4$). The definition of numerical source $\boldsymbol{\Phi}_k$ is analogous to $\boldsymbol{F}_k$. The utilization of interface values aids in preserving the well-balanced property with scarcely increased numerical difficulties.

Plugging (2.10) and (2.11) into (2.9), we get a semi-discrete adaptation of (2.2),

$$\frac{\mathrm{d}}{\mathrm{d}t}\left(\overline{\boldsymbol{U}}_{i,j}|\Omega_{i,j}|\right)=-\sum_{k=1,2,3,4}\boldsymbol{F}_k|\mathcal{S}_k|+\frac{|\Omega_{i,j}|}{r_{i,j}}\boldsymbol{\Sigma}_{i,j}.$$

Employ the midpoint rule for time advancement, then the full discretization is achieved:

$$\overline{\boldsymbol{U}}_{i,j}^{n+1}=\frac{|\Omega_{i,j}^n|}{|\Omega_{i,j}^{n+1}|}\overline{\boldsymbol{U}}_{i,j}^n-\frac{\Delta t^n}{|\Omega_{i,j}^{n+1}|}\sum_{k=1,2,3,4}\boldsymbol{F}_k^{n+\frac{1}{2}}|\mathcal{S}_k^{n+\frac{1}{2}}|+\Delta t^n\cdot\frac{|\Omega_{i,j}^{n+\frac{1}{2}}|}{|\Omega_{i,j}^{n+1}|}\frac{\boldsymbol{\Sigma}_{i,j}^{n+\frac{1}{2}}}{r_{i,j}^{n+\frac{1}{2}}}. \tag{2.12}$$

Herein the superscript n signifies the value at the n-th time level $t=t^n$, with the time increment $\Delta t^n=t^{n+1}-t^n$ and the middle level $t^{n+1/2}=t^n+\Delta t^n/2$.

We have derived the cell-centered Lagrangian scheme (2.12) of axisymmetric fluids under the 3D view. It can be exploited as a consistent boundary treatment at $r=0$ because we have circumvented the singularity of $\boldsymbol{\Phi}/r$. As matters stand, three issues will be focused on later.

(i) How to construct the numerical flux $\boldsymbol{F}_k^{n+1/2}$ and source $\boldsymbol{\Phi}_k^{n+1/2}$? We will propose the GRP solvers in Section 3 for an "interchange" variable $\widetilde{\boldsymbol{V}}_k^{n+1/2}$ to address it.

(ii) How to calculate geometrical quantities $|\Omega_{i,j}^{n+1/2}|$, $|\Omega_{i,j}^{n+1}|$, and $|\mathcal{S}_k^{n+1/2}|$? They can be derived from the vertex positions $\boldsymbol{x}_{i\pm1/2,j\pm1/2}^{n+1/2}$ and $\boldsymbol{x}_{i\pm1/2,j\pm1/2}^{n+1}$, $i\in\mathbb{N}$, $j\in\mathbb{Z}$. Thereby we will put forward a nine-point least-squares method in Section 4.1 for the velocity $\boldsymbol{u}_{i\pm1/2,j\pm1/2}^{n}$ and the acceleration $(\mathrm{d}\boldsymbol{u}/\mathrm{d}t)_{i\pm1/2,j\pm1/2}^{n}$.

(iii) The underlying midpoint velocities $\boldsymbol{u}_{i\pm1/2,j}^{n+1/2}$ and $\boldsymbol{u}_{i,j\pm1/2}^{n+1/2}$ in (i) are supposed to match the vertex velocities $\boldsymbol{u}_{i\pm1/2,j\pm1/2}^{n+1/2}$ in (ii), $i\in\mathbb{N}$, $j\in\mathbb{Z}$. We will slightly modify $\widetilde{\boldsymbol{V}}_k^{n+1/2}$ in Section 4.2 to reach this with the help of axisymmetric GCL constraint.

3 The axisymmetric GRP solvers

Suppose that at time $t=t^n$, $\boldsymbol{V}(r,z,t^n)$ is distributed piece-wise linearly,

$$\boldsymbol{V}(r,z,t^n)=\overline{\boldsymbol{V}}_{i,j}^n+\boldsymbol{\varsigma}_{i,j}^n\cdot(\boldsymbol{x}-\boldsymbol{x}_{i,j}^n)^T,\quad \boldsymbol{x}\in\mathcal{K}_{i,j}(t^n), \tag{3.1}$$

among which $\overline{\boldsymbol{V}}_{i,j}^n=\boldsymbol{V}(\overline{\boldsymbol{U}}_{i,j}^n)$, $\boldsymbol{\varsigma}=[\boldsymbol{\varsigma}_r,\boldsymbol{\varsigma}_z]_{4\times2}=[\partial\boldsymbol{V}/\partial r,\partial\boldsymbol{V}/\partial z]$ is the gradient tensor of $\boldsymbol{V}$. In this section, we separate the GRP solvers for the normal variable values $\widetilde{\boldsymbol{V}}_{i-1/2,j}^{n+1/2}$ ($i\in\mathbb{N}$) into two scenarios: the one for $\widetilde{\boldsymbol{V}}_{i-1/2,j}^{n+1/2}$ ($i\in\mathbb{N}^*$) at the interior interfaces and the other for $\widetilde{\boldsymbol{V}}_{-1/2,j}^{n+1/2}$ at the symmetric axis $r=0$. The same goes for $\widetilde{\boldsymbol{V}}_{i,j-1/2}^{n+1/2}$.

3.1 Interior interface values

The exposition is made in three steps: (i) Derive the local Eulerian system about $\widetilde{\boldsymbol{V}}$ along the interface normal $\boldsymbol{n}$. (ii) Convert it to the Lagrangian type. (iii) Formulate the initial condition of the GRP and supply concrete content of its solver.

(i) Local rotated Eulerian system

Paired with $\boldsymbol{n}=(n_r,n_z)$ and $\widetilde{u}$, we denote the interface tangential vector and velocity as $\boldsymbol{t}=(-n_z,n_r)$ and $\widetilde{v}$. These four can be linked together by a unit orthogonal matrix $\boldsymbol{N}$,

$$(\widetilde{u},\widetilde{v})^T=\boldsymbol{N}\cdot(u,v)^T,\quad \boldsymbol{N}=\begin{bmatrix}\cdot\,\boldsymbol{n}\,\cdot\\ \cdot\,\boldsymbol{t}\,\cdot\end{bmatrix}=\begin{bmatrix}n_r & n_z\\ -n_z & n_r\end{bmatrix},\quad \boldsymbol{N}^{-1}=\boldsymbol{N}^T.$$

The local coordinate $\boldsymbol{\zeta}=(\xi,\eta)$ is the projection of $\boldsymbol{x}=(r,z)$ to $\boldsymbol{n}$ and $\boldsymbol{t}$,

$$(\xi,\eta)^T=\boldsymbol{N}\cdot(r,z)^T,\quad \text{i.e.}\quad \boldsymbol{\zeta}^T=\boldsymbol{N}\boldsymbol{x}^T. \tag{3.2}$$

Out of the misalignment between the directions of $\boldsymbol{u}=(u,v)$ and $\boldsymbol{n}$, we redefine the local flow system. The variable rotation is fulfilled using a block diagonal matrix $\boldsymbol{M}$,

$$\widetilde{\boldsymbol{V}}=\boldsymbol{M}\boldsymbol{V}=[\rho,\widetilde{u},\widetilde{v},p]^T,\quad \boldsymbol{M}=\mathrm{diag}(1,\boldsymbol{N},1). \tag{3.3}$$

Multiplying the system (2.5) by $\boldsymbol{M}$, we acquire its new interpretation around $\widetilde{\boldsymbol{V}}(\xi,\eta,t)$,

$$\frac{\partial \widetilde{\boldsymbol{V}}}{\partial t}+\boldsymbol{G}(\widetilde{\boldsymbol{V}})\frac{\partial \widetilde{\boldsymbol{V}}}{\partial \xi}+\boldsymbol{H}(\widetilde{\boldsymbol{V}})\frac{\partial \widetilde{\boldsymbol{V}}}{\partial \eta}=\boldsymbol{\Psi}(\xi,\eta,\widetilde{\boldsymbol{V}}), \tag{3.4}$$

with the matrices $\boldsymbol{G}(\widetilde{\boldsymbol{V}})$ and $\boldsymbol{H}(\widetilde{\boldsymbol{V}})$ being

$$\boldsymbol{G}(\widetilde{\boldsymbol{V}})=n_r\boldsymbol{M}\boldsymbol{G}(\boldsymbol{V})\boldsymbol{M}^T+n_z\boldsymbol{M}\boldsymbol{H}(\boldsymbol{V})\boldsymbol{M}^T,\quad \boldsymbol{H}(\widetilde{\boldsymbol{V}})=-n_z\boldsymbol{M}\boldsymbol{G}(\boldsymbol{V})\boldsymbol{M}^T+n_r\boldsymbol{M}\boldsymbol{H}(\boldsymbol{V})\boldsymbol{M}^T.$$

The source term $\boldsymbol{\Psi}(r,\boldsymbol{V})$ in (2.5) conforms to the rotational invariance: $\boldsymbol{M}\boldsymbol{\Psi}=\boldsymbol{\Psi}$. Using (3.2) and (3.3), it can be transformed via

$$\boldsymbol{\Psi}(r,\boldsymbol{V})=\boldsymbol{\Psi}\big(r(\xi,\eta),\boldsymbol{V}(\xi,\eta,\widetilde{\boldsymbol{V}})\big). \tag{3.5}$$

For simplicity, we denote the right representation as $\boldsymbol{\Psi}(\xi,\eta,\widetilde{\boldsymbol{V}})$. Such is the case with (3.4).

Fixing η, the ξ-split of the system (3.4) writes:

$$\frac{\partial \widetilde{\boldsymbol{V}}}{\partial t}+\boldsymbol{G}(\widetilde{\boldsymbol{V}})\frac{\partial \widetilde{\boldsymbol{V}}}{\partial \xi}=\boldsymbol{\Psi}_1(\xi,\widetilde{\boldsymbol{V}}),\quad \boldsymbol{\Psi}_1=-\frac{n_r}{r(\xi)}[\rho\widetilde{u},0,0,\rho c^2\widetilde{u}]^T. \tag{3.6}$$

Remark 3.1. The systems (2.3), (2.5), and (3.4) will actually describe 2D planar flows if the source terms $\boldsymbol{\Phi}$ and $\boldsymbol{\Psi}$ are dropped. This deviates from our topic. Moreover, the splitting of $\boldsymbol{\Psi}(\xi,\eta,\widetilde{\boldsymbol{V}})$ is the key to the dimensional splitting of (3.4). Our practice mainly bases on the concern that the system (3.6) can revert to a radially symmetric fluid model,

$$\frac{\partial \boldsymbol{V}}{\partial t}+\boldsymbol{G}(\boldsymbol{V})\frac{\partial \boldsymbol{V}}{\partial r}=\boldsymbol{\Psi}(r,\boldsymbol{V}), \tag{3.7}$$

when $\boldsymbol{n}=(\pm1,0)$ (Fig. 1(c)). Our Lagrangian GRP solver shall be convertible to the 1D Eulerian one in [19] under such condition.

(ii) Euler–Lagrange mapping

At time $t=t^n$, concentrating on $\zeta^n_{i-1/2,j}$ and letting $\eta=\eta^n_{i-1/2,j}$, we define the Lagrangian coordinate of the particle located at ξ as

$$\Xi:=\int_{\zeta^n_{i-\frac{1}{2},j}}^{\xi} n_r(sn_r-\eta^n_{i-\frac{1}{2},j}n_z)\cdot\rho(s,t^n)ds. \tag{3.8}$$

It stands for the total mass enclosed in the duct section $s\in[\zeta^n_{i-1/2,j},\xi]$, which is shaped like an annulus when $\boldsymbol{n}=(\pm1,0)$.

Assuming that the particle paths issuing from different positions do not intersect with each other during the time interval $t\in[t^n,t^{n+1})$, the mapping $\Xi\to\xi(\Xi,t)$ and its inverse $\xi\to\Xi(\xi,t)$ are well defined. Thus we have

$$\frac{\partial \xi}{\partial t}(\Xi,t)=\widetilde{u}(\Xi,t). \tag{3.9}$$

Just like (3.5), a flow variable Q can be expressed in both the Eulerian form $Q(\xi,t)$ and the Lagrangian form $Q(\Xi,t)$.

Using (3.9), the time derivative of $Q(\Xi,t)$ is

$$\frac{\partial Q}{\partial t}(\Xi,t)=\frac{\partial Q}{\partial t}(\xi,t)\bigg|_{\xi=\xi(\Xi,t)}+\widetilde{u}(\Xi,t)\frac{\partial Q}{\partial \xi}(\xi,t)\bigg|_{\xi=\xi(\Xi,t)},$$

which is identical to the total derivative $\mathrm{d}Q/\mathrm{d}t(\xi,t)$. Drawing on (3.2) and (3.8), we know

$$\frac{\partial \xi}{\partial \Xi}(\Xi,t)=\left[n_r r(\Xi,t)\rho(\Xi,t)\right]^{-1}. \tag{3.10}$$

With the above two equations, the Lagrangian formalism of the system (3.6) is

$$\frac{\partial \widetilde{\boldsymbol{V}}}{\partial t}+\boldsymbol{A}(\widetilde{\boldsymbol{V}})\frac{\partial \widetilde{\boldsymbol{V}}}{\partial \Xi}=\boldsymbol{\Psi}_1(\Xi,\widetilde{\boldsymbol{V}}),\quad \boldsymbol{A}(\widetilde{\boldsymbol{V}})=n_r r\rho\big(\boldsymbol{G}(\widetilde{\boldsymbol{V}})-\widetilde{u}\boldsymbol{I}\big), \tag{3.11}$$

where $\boldsymbol{I}$ is the identity matrix. All of the flow variables, as well as the coordinate r, are functions of Ξ and t.

(iii) Specifics of the GRP solver

Shift our attention to a couple of adjacent cells $\mathcal{K}^n_{i-1,j}$ and $\mathcal{K}^n_{i,j}$. According to (3.1), the variable $\boldsymbol{V}(r,z,t^n)$ is distributed as

$$\boldsymbol{V}(r,z,t^n)=\begin{cases}\overline{\boldsymbol{V}}^n_{i,j}+\boldsymbol{\varsigma}^n_{i,j}\cdot(\boldsymbol{x}-\boldsymbol{x}^n_{i,j})^T, & \boldsymbol{x}\in\mathcal{K}^n_{i,j},\\ \overline{\boldsymbol{V}}^n_{i-1,j}+\boldsymbol{\varsigma}^n_{i-1,j}\cdot(\boldsymbol{x}-\boldsymbol{x}^n_{i-1,j})^T, & \boldsymbol{x}\in\mathcal{K}^n_{i-1,j},\end{cases}$$

in them. From the standpoint of $\boldsymbol{x}^n_{i-1/2,j}$ on $\mathcal{K}^n_{i,j}$, the rotated $\widetilde{\boldsymbol{V}}(\xi,\eta,t^n)$ on both sides of the interface is distributed as

$$\widetilde{\boldsymbol{V}}(\xi,\eta,t^n)=\begin{cases}\widetilde{\boldsymbol{V}}_1(\xi,\eta):=\boldsymbol{M}\overline{\boldsymbol{V}}^n_{i,j}+\boldsymbol{\sigma}^n_{i,j}\cdot(\boldsymbol{\zeta}-\boldsymbol{\zeta}^n_{i,j})^T, & \xi<\xi^n_{i-\frac{1}{2},j},\\ \widetilde{\boldsymbol{V}}_2(\xi,\eta):=\boldsymbol{M}\overline{\boldsymbol{V}}^n_{i-1,j}+\boldsymbol{\sigma}^n_{i-1,j}\cdot(\boldsymbol{\zeta}-\boldsymbol{\zeta}^n_{i-1,j})^T, & \xi>\xi^n_{i-\frac{1}{2},j},\end{cases}$$

where $\boldsymbol{\sigma}$ is the gradient tensor of $\widetilde{\boldsymbol{V}}$. Using (3.2) and (3.3), it can relate to $\boldsymbol{\varsigma}$ by

$$\boldsymbol{\sigma}=[\boldsymbol{\sigma}_\xi,\boldsymbol{\sigma}_\eta]_{4\times 2}=\left[\frac{\partial \widetilde{\boldsymbol{V}}}{\partial \xi},\frac{\partial \widetilde{\boldsymbol{V}}}{\partial \eta}\right]=\boldsymbol{M}\boldsymbol{\varsigma}\boldsymbol{N}^T.$$

As displayed in Fig. 3, we can complete the Euler–Lagrange transformation of the variable $\widetilde{\boldsymbol{V}}$ on the $\eta=\eta^n_{i-1/2,j}$ plane by (3.8) and (3.10),

$$\widetilde{\boldsymbol{V}}(\Xi,\eta^n_{i-\frac{1}{2},j},t^n)=\begin{cases}\widetilde{\boldsymbol{V}}_-(\Xi):=\widetilde{\boldsymbol{V}}_L+\widetilde{\boldsymbol{V}}'_L\Xi, & \Xi<0,\\ \widetilde{\boldsymbol{V}}_+(\Xi):=\widetilde{\boldsymbol{V}}_R+\widetilde{\boldsymbol{V}}'_R\Xi, & \Xi>0,\end{cases} \tag{3.12}$$

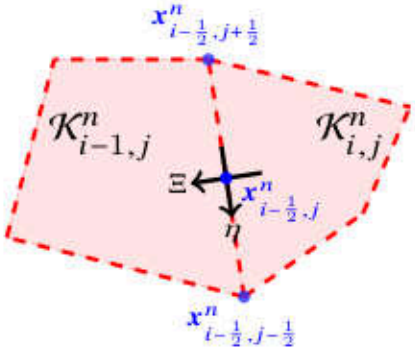

Fig. 3: The localization of $x^n_{i-1/2,j}$ ($i\in\mathbb{N}^*$) viewed from $\mathcal{K}^n_{i,j}$.

wherein $\widetilde{V}_J$ and $\widetilde{V}'_J$ ($J=L$ or R) are prearranged as

$$\widetilde{V}_L := \lim_{\Xi\to 0-} \widetilde{V}_1(\Xi,\eta^n_{i-\frac{1}{2},j}), \quad \widetilde{V}'_L(\Xi) := \frac{(\sigma_\xi)^n_{i,j}}{n_r r\rho(\Xi,\eta^n_{i-\frac{1}{2},j},t^n)},$$
$$\widetilde{V}_R := \lim_{\Xi\to 0+} \widetilde{V}_2(\Xi,\eta^n_{i-\frac{1}{2},j}), \quad \widetilde{V}'_R(\Xi) := \frac{(\sigma_\xi)^n_{i-1,j}}{n_r r\rho(\Xi,\eta^n_{i-\frac{1}{2},j},t^n)}.$$

The GRP of our interest is a Cauchy problem for (3.11) subject to the initial condition (3.12). The interior interface values $\widetilde{V}^{n+1/2}_{i-1/2,j}$ ($i\in\mathbb{N}^*$) are obtained through resolving it at $(\Xi,\eta,t)=(0,\eta^n_{i-1/2,j},t^n)$. Specifically, we approximate them with second-order accuracy:

$$\widetilde{V}^{n+\frac{1}{2}}_{i-\frac{1}{2},j} \approx \widetilde{V}^{n,*}_{i-\frac{1}{2},j} + \frac{\Delta t}{2}\left(\frac{\partial\widetilde{V}}{\partial t}\right)^{n,*}_{i-\frac{1}{2},j}, \quad i\in\mathbb{N}^*, \tag{3.13}$$

of which the two decisive components are the instantaneous values of the solution and its temporal derivative at the initial discontinuity $\Xi=0$,

$$\widetilde{V}^{n,*}_{i-\frac{1}{2},j} := \lim_{t\to t^n+} \widetilde{V}(0,\eta^n_{i-\frac{1}{2},j},t), \quad \left(\frac{\partial\widetilde{V}}{\partial t}\right)^{n,*}_{i-\frac{1}{2},j} := \lim_{t\to t^n+} \frac{\partial\widetilde{V}}{\partial t}(0,\eta^n_{i-\frac{1}{2},j},t).$$

We simply refer to them as $\widetilde{V}_*$ and $(\partial\widetilde{V}/\partial t)_*$ here-in-after. The former is the solution to the associated Riemann problem along $\Xi=0$. We illustrate the differences and similarities between it and the GRP in Fig. 4. Details can be found in [5,32].

On the flip side, using the Lax–Wendroff procedure, the resolution of $(\partial\widetilde{V}/\partial t)_*$ resembles other GRP studies in [4]. The critical piece is to derive a pair of linear relations

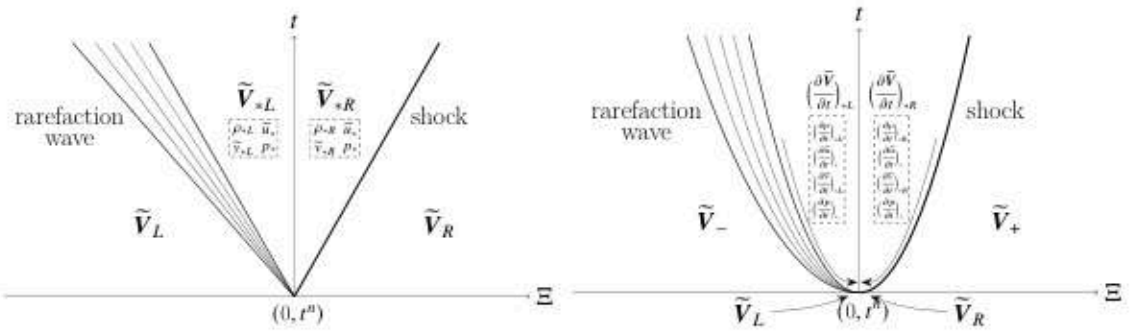

Fig. 4: The comparison of a possible wave pattern on the $\eta=\eta^n_{i-1/2,j}$ plane. Left: the associated Riemann problem, right: the GRP (3.11) and (3.12). Since ρ jumps discontinuously across the t-axis, we append it and its time derivative $\partial\rho/\partial t$ a subscript J ($J=L$ or R) for differentiation, for example $\rho_{*L}:=\lim_{t\to t^n+}\rho(0-,\eta^n_{i-1/2,j},t)$. The same applies to $\widetilde{v}$.

concerning the Lagrangian derivatives $(\partial\widetilde{u}/\partial t)_*$ and $(\partial p/\partial t)_*$,

$$\begin{aligned} a_L\left(\frac{\partial\widetilde{u}}{\partial t}\right)_*+b_L\left(\frac{\partial p}{\partial t}\right)_*&=d_L,\\ a_R\left(\frac{\partial\widetilde{u}}{\partial t}\right)_*+b_R\left(\frac{\partial p}{\partial t}\right)_*&=d_R, \end{aligned} \tag{3.14}$$

where the coefficients a_J, b_J, and d_J are constants depending on $\widetilde{\boldsymbol{V}}_J$ and $\widetilde{\boldsymbol{V}}'_J(0\pm)$ ($J=L$ or R). The deduction process is omitted. Still, to make our paper self-contained, their values in all instances are concluded in Appendix. The readers only need to consult it when implementing our GRP solver. After $(\partial p/\partial t)_*$ is settled down, the values of $(\partial\rho/\partial t)_{*J}$ and $(\partial\widetilde{v}/\partial t)_*$ can be easily gotten by (3.11),

$$\left(\frac{\partial\rho}{\partial t}\right)_{*J}=\frac{1}{c^2_{*J}}\left(\frac{\partial p}{\partial t}\right)_*,\quad \left(\frac{\partial\widetilde{v}}{\partial t}\right)_{*J}=0,\quad J=L\text{ or }R.$$

So far, we have finished the resolution of interior interface values $\widetilde{\boldsymbol{V}}^{n+1/2}_{i-1/2,j}$ ($i\in\mathbb{N}^*$).

3.2 Inner boundary values at the symmetric axis

Notice that for the boundary value $\widetilde{\boldsymbol{V}}^{n+1/2}_{-1/2,j}$ at $r=0$, the local coordinates (ξ,η) are mirrored to (r,z) and $\boldsymbol{n}=(-1,0)$. We opt to evaluate it by $\boldsymbol{V}^{n+1/2}_{-1/2,j}$.

As mentioned in Remark 2.2, the interface initially located at the axis $r=0$ can never escape from there. Thus we obtain the value $\boldsymbol{V}^{n+1/2}_{-1/2,j}$ by resolving the one-sided GRP at $(r,z,t)=(0,z^n_{-1/2,j},t^n)$. It is a Dirichlet problem for (3.7) subject to the initial data

$$\boldsymbol{V}(r,z,t^n)=\boldsymbol{V}_+(r,z):=\overline{\boldsymbol{V}}^n_{0,j}+\boldsymbol{\varsigma}^n_{0,j}\cdot(\boldsymbol{x}-\boldsymbol{x}^n_{0,j})^T \tag{3.15}$$

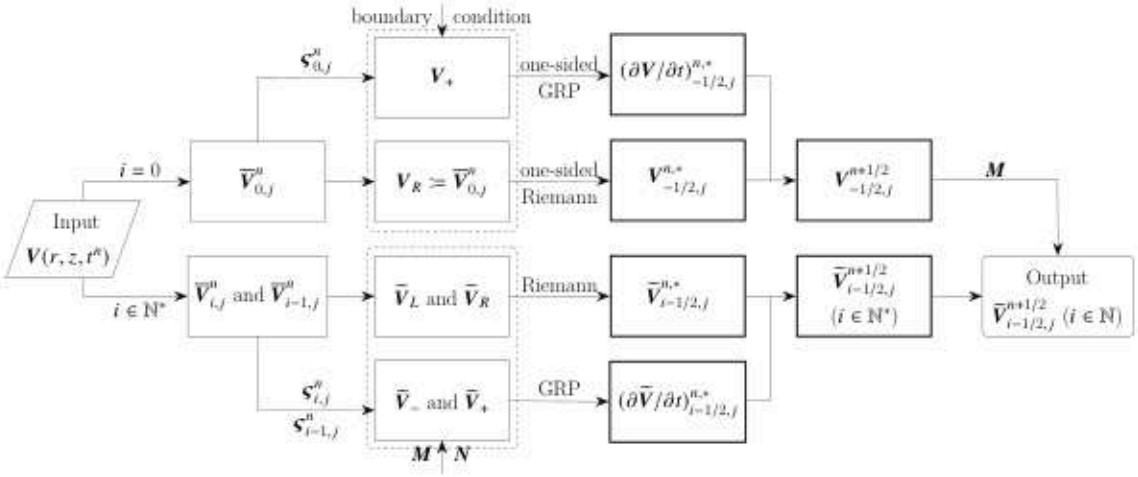

Fig. 5: The flow sheet of calculating the interface values $\widetilde{\boldsymbol{V}}^{n+1/2}_{i-1/2,j}$ $(i\in\mathbb{N})$.

and the boundary condition (2.8). The corresponding solver is referred to our past research in [39]. Its heart resides in employing the L'Hospital's rule to transfer the singular term u/r into the space derivative $\partial u/\partial r$. We will demonstrate in Section 6 that the combination of this solver and the brand-new numerical boundary condition (2.12) owns an edge when compared with the reflective one.

For ease of understanding, the main bits of our axisymmetric GRP solvers for $\widetilde{\boldsymbol{V}}^{n+1/2}_{i-1/2,j}$ $(i\in\mathbb{N})$ are refined in Fig. 5.

4 The Lagrangian computing mesh

This section is devoted to tracking the Lagrangian mesh motion. We analyze it from two aspects. On the one hand, the evolution of cells is driven by the movement of vertices. It calls for calculating their velocities with the interface normal ones acquired in Section 3. On the other hand, these two classes of velocities should be compatible with each other. We choose to repair the potential "mismatch" by virtue of the GCL.

4.1 Nine-point least-squares method

As for calculating the interior vertex velocities $\boldsymbol{u}^n_{i-1/2,j+1/2}$ $(i\in\mathbb{N}^*,\ j\in\mathbb{Z})$, we retrospect the five- and thirteen-point least-squares methods raised in [1,29], see the left two panels of Fig. 6. The latter counts the four 2D cells that share the vertex $\boldsymbol{x}^n_{i-1/2,j+1/2}$ as a whole linear area with respect to the velocity $\boldsymbol{u}$. It involves the information of twelve midpoints

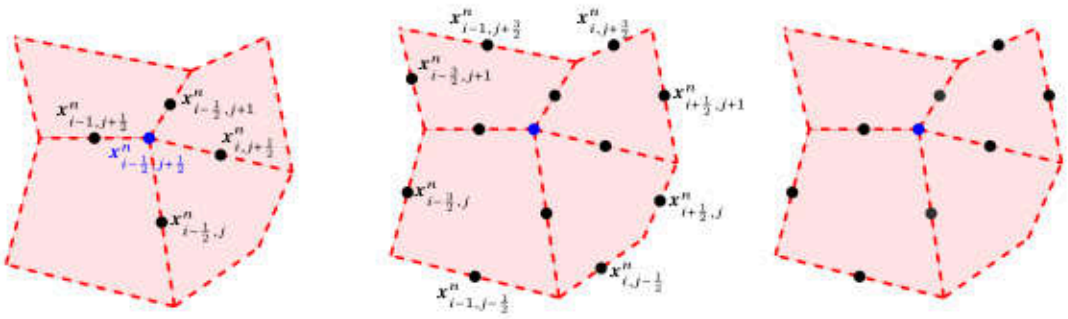

Fig. 6: The computational stencils of three least-squares methods for the objective velocity $\boldsymbol{u}^n_{i-1/2,j+1/2}$, with the vertex $\boldsymbol{x}^n_{i-1/2,j+1/2}$ colored in blue. Left: five-point [1], middle: thirteen-point [29], right: our nine-point.

and six unknowns, i.e. $\boldsymbol{u}^n_{i-1/2,j+1/2}$ and $(\nabla \boldsymbol{u})^n_{i-1/2,j+1/2}$. The functional to minimize is

$$\sum_{p=i-1,i}\sum_{q=j\pm\frac{1}{2},j+\frac{3}{2}} w_{p,q}\left\{\left[\boldsymbol{u}^n_{i-\frac{1}{2},j+\frac{1}{2}}+(\boldsymbol{x}^n_{p,q}-\boldsymbol{x}^n_{i-\frac{1}{2},j+\frac{1}{2}})\cdot(\nabla\boldsymbol{u})^n_{i-\frac{1}{2},j+\frac{1}{2}}\right]\cdot\boldsymbol{n}_{p,q}-\widetilde{u}^{n,*}_{p,q}\right\}^2$$
$$+\sum_{p=i-\frac{3}{2},i\pm\frac{1}{2}}\sum_{q=j,j+1} w_{p,q}\left\{\left[\boldsymbol{u}^n_{i-\frac{1}{2},j+\frac{1}{2}}+(\boldsymbol{x}^n_{p,q}-\boldsymbol{x}^n_{i-\frac{1}{2},j+\frac{1}{2}})\cdot(\nabla\boldsymbol{u})^n_{i-\frac{1}{2},j+\frac{1}{2}}\right]\cdot\boldsymbol{n}_{p,q}-\widetilde{u}^{n,*}_{p,q}\right\}^2. \quad (4.1)$$

Herein $\boldsymbol{n}_{p,q}$ and $w_{p,q}$ are the direction and the weight of the Riemann velocity $\widetilde{u}^{n,*}_{p,q}$ that has shown up in (3.13). Whereas the five-point method is established on the constant field.

Notably, these two methods indiscriminately absorb the midpoints all around. It may mix the velocity components and confuse the flow direction. In addition, we would like to reduce computational costs and errors of the thirteen-point method. Our nine-point edition is thus born. It avoids the area with significant velocity variation.

Its stencil firstly includes the four midpoints closely adjacent to $\boldsymbol{x}^n_{i-1/2,j+1/2}$. As to the above-mentioned four cells, the rest four peripheral midpoints are picked from the two of them with the smallest $\|\nabla\boldsymbol{u}\|$ value. The matrix norm is designed for measuring the degree of discontinuity. We usually take it as the Frobenius one and adopt the difference approximation in [28] to quantify it.

A probable case is offered in the rightmost subfigure of Fig. 6. Eight degrees of freedom are taken into (4.1) to determine $\boldsymbol{u}^n_{i-1/2,j+1/2}$. To some extent, our method can be seen as a rough "deep neural network" version of the thirteen-point one. The activation function is relevant to $\|\nabla\boldsymbol{u}\|$.

The comparisons between these three methods are given in 6.1. We can calculate the vertex acceleration $(\mathrm{d}\boldsymbol{u}/\mathrm{d}t)^n_{i-1/2,j+1/2}$ analogously from the interface GRP accelerations in (3.13).

Remark 4.1. The linear estimation of vertex velocity synchronizes with our scheme (2.12). A question arises: Can the stencil be more compact? We fear that the answer might be

no. A linear field of $\boldsymbol{u}$ demands at least six degrees of freedom for determination. Yet the resultant 6×6 system will be singular on a rectangular mesh. Meanwhile, we observe that it is better to select equal numbers of midpoints on the r- and z-sides in practice. Otherwise the system may be ill-conditioned. These support our idea on the other side.

4.2 Axisymmetric GCL modification

The GCL plays an important role in designing the Lagrangian algorithms, while the vertex velocities educed by the least-squares method might break it. So we turn back to modify the interface normal ones. The pressure there will change a little bit accordingly.

The integral interpretation of the axisymmetric GCL can be expressed as

$$\frac{\mathrm{d}}{\mathrm{d}t}\iiint_{\Omega(t)} r\mathrm{d}r\mathrm{d}\theta\mathrm{d}z-\iint_{\partial\Omega(t)}\widetilde{u}\mathrm{d}S=0.$$

Using (2.6), we unfold the volume integral of the 3D cell $\Omega_{i,j}$ in Fig. 1(b),

$$\begin{aligned}\frac{\mathrm{d}|\Omega_{i,j}|}{\mathrm{d}t}=\frac{\pi}{3}\sum_{k=1}^{4}\big[&u_{k+1}(2r_{k+1}+r_k)\cdot(z_{k+1}-z_k)+u_k(r_{k+1}+2r_k)\cdot(z_{k+1}-z_k)\\&+v_{k+1}(r_{k+1}^2+r_{k+1}r_k+r_k^2)-v_k(r_{k+1}^2+r_{k+1}r_k+r_k^2)\big].\end{aligned}$$

Rearrange the last two terms by minus and plus the sum of $3v_kr_k^2$. It gives rise to

$$\begin{aligned}\frac{\mathrm{d}|\Omega_{i,j}|}{\mathrm{d}t}=\frac{\pi}{3}\sum_{k=1}^{4}\big[&u_{k+1}(2r_{k+1}+r_k)\cdot(z_{k+1}-z_k)+u_k(r_{k+1}+2r_k)\cdot(z_{k+1}-z_k)\\&+v_{k+1}(2r_{k+1}+r_k)\cdot(r_k-r_{k+1})+v_k(r_{k+1}+2r_k)\cdot(r_k-r_{k+1})\big].\end{aligned}$$

Comparing the above equation with (2.7), we can get the interface normal velocities in line with the vertex ones. At $t=t^{n+1/2}$, a manifestation of the relation is

$$\widetilde{u}^{n+\frac{1}{2},\star}_{i-\frac{1}{2},j}=\frac{\left(2r^{n+\frac{1}{2}}_{i-\frac{1}{2},j-\frac{1}{2}}+r^{n+\frac{1}{2}}_{i-\frac{1}{2},j+\frac{1}{2}}\right)\boldsymbol{u}^{n+\frac{1}{2}}_{i-\frac{1}{2},j-\frac{1}{2}}+\left(r^{n+\frac{1}{2}}_{i-\frac{1}{2},j-\frac{1}{2}}+2r^{n+\frac{1}{2}}_{i-\frac{1}{2},j+\frac{1}{2}}\right)\boldsymbol{u}^{n+\frac{1}{2}}_{i-\frac{1}{2},j+\frac{1}{2}}}{3\left(r^{n+\frac{1}{2}}_{i-\frac{1}{2},j-\frac{1}{2}}+r^{n+\frac{1}{2}}_{i-\frac{1}{2},j+\frac{1}{2}}\right)}\cdot\boldsymbol{n}^{n+\frac{1}{2}}_{i-\frac{1}{2},j},\quad i\in\mathbb{N}^*.$$

Incidentally, the boundary velocity at the axis $r=0$ automatically satisfies the GCL since we have preset $\widetilde{u}^{n+1/2}_{-1/2,j}=0$ in our one-sided GRP solver.

Inspired by other approximate Riemann solvers in [26, 32], we revise the interface pressure to

$$p^{n+\frac{1}{2},\star}_{i-\frac{1}{2},j}=\frac{1}{2}\left(\rho^{n+\frac{1}{2},R}_{i-\frac{1}{2},j}c^{n+\frac{1}{2},R}_{i-\frac{1}{2},j}-\rho^{n+\frac{1}{2},L}_{i-\frac{1}{2},j}c^{n+\frac{1}{2},L}_{i-\frac{1}{2},j}\right)\cdot\left(\widetilde{u}^{n+\frac{1}{2},\star}_{i-\frac{1}{2},j}-\widetilde{u}^{n+\frac{1}{2}}_{i-\frac{1}{2},j}\right)+p^{n+\frac{1}{2}}_{i-\frac{1}{2},j},\ i\in\mathbb{N}^*,$$

where $\widetilde{u}^{n+1/2}_{i-1/2,j}$ and $p^{n+1/2}_{i-1/2,j}$ have appeared earlier in (3.13). The superscript J of $\rho^{n+1/2,J}_{i-1/2,j}$ and $c^{n+1/2,J}_{i-1/2,j}$ ($J=L$ or R) has been introduced beforehand in the caption of Fig. 4.

The above two equations ultimately constitute the modification of the numerical flux $\boldsymbol{F}^{n+1/2}_{i-1/2,j}$ and source $\boldsymbol{\Phi}^{n+1/2}_{i-1/2,j}$ in (2.12). The same works with $\boldsymbol{F}^{n+1/2}_{i,j-1/2}$ and $\boldsymbol{\Phi}^{n+1/2}_{i,j-1/2}$.

5 Summarization of the axisymmetric GRP algorithm

It is time to piece Sections 2-4 together and present a complete story about our axisymmetric GRP algorithm. We outline its major steps in the view of $\Omega_{i,j}$ ($i\in\mathbb{N}$) as follows. The first three steps echo the three questions put forward at the end of Section 2.

Step 1. At time $t=t^n$, $\boldsymbol{V}(r,z,t^n)$ exhibits a piece-wise linear distribution (3.1). Obtain the interior interface values $\widetilde{\boldsymbol{V}}^{n+1/2}_{i\pm1/2,j}$ (if $i\in\mathbb{N}^*$) and $\widetilde{\boldsymbol{V}}^{n+1/2}_{i,j\pm1/2}$ by the GRP solver. Obtain the boundary value $\widetilde{\boldsymbol{V}}^{n+1/2}_{-1/2,j}$ (if $i=0$) by the one-sided GRP solver.

Step 2. Compute the vertex velocities $\boldsymbol{u}^n_{i\pm1/2,j\pm1/2}$ and accelerations $(\mathrm{d}\boldsymbol{u}/\mathrm{d}t)^n_{i\pm1/2,j\pm1/2}$ by the nine-point least-squares method. Use the motion equation $d\boldsymbol{x}/dt=\boldsymbol{u}$ to determine the locations $\boldsymbol{x}^{n+1/2}_{i\pm1/2,j\pm1/2}$ and $\boldsymbol{x}^{n+1}_{i\pm1/2,j\pm1/2}$, such as

$$\boldsymbol{x}^{n+1}_{i\pm\frac{1}{2},j\pm\frac{1}{2}}=\boldsymbol{x}^{n}_{i\pm\frac{1}{2},j\pm\frac{1}{2}}+\Delta t^n\boldsymbol{u}^n_{i\pm\frac{1}{2},j\pm\frac{1}{2}}+\frac{(\Delta t^n)^2}{2}\left(\frac{\mathrm{d}\boldsymbol{u}}{\mathrm{d}t}\right)^n_{i\pm\frac{1}{2},j\pm\frac{1}{2}}.$$

Substitute them into (2.6) and (2.7) to attain $|\Omega^{n+1/2}_{i,j}|$, $|\Omega^{n+1}_{i,j}|$, and $|\mathcal{S}^{n+1/2}_k|$, $k=1,2,3,4$.

Step 3. Modify the normal velocity and pressure parts of $\widetilde{\boldsymbol{V}}^{n+1/2}_{i\pm1/2,j}$ and $\widetilde{\boldsymbol{V}}^{n+1/2}_{i,j\pm1/2}$ by the axisymmetric GCL constraint. Update the cell average $\overline{\boldsymbol{U}}^{n+1}_{i,j}$ with the iterative formula (2.12). Transmissive boundary conditions will be applied to the other boundaries unless otherwise noted.

Step 4. Reconstruct the gradient $\varsigma^{n+1}_{i,j}$ globally by the Barth–Jespersen limiter [2]. Return to *Step 1* until $t=T$.

6 Numerical examples

With the entire algorithm coming into the picture, we are in the position to check its performance. The kernel recurrence formula (2.12) serves a dual purpose: the numerical boundary condition and the scheme on interior cells. We use the results obtained by the modified Dukowicz solver in [33, 34] (labelled with "**Vilar**" in the graph legend) as references. It has already been successfully applied to the research of symmetric flows in [20]. Besides, we set a control group: the results under the alliance of our scheme and reflective boundary condition (labelled with "**Reflective**") in the following tests. The magnitude of Δt^n is limited by the CFL stability criterion with $\nu_{CFL}=0.6$.

6.1 Test of our nine-point least-squares method

Here we estimate the accuracy and effectiveness of our nine-point least-squares method. This is achieved by comparing it with the other two methods introduced in Section 4.1 on diverse meshes and velocity fields.

Divide the computational domain $[0.5,1.5]\times[0.5,1.5]$ into N^2 square cells with the side length h. Keep boundary vertices still. Move the internal ones to deform the mesh into two types, "smooth" and random, as detailed below.

The vertices of the first "smooth" mesh correspond with the original (R,Z) by

$$r(R,Z)=R+0.1\sin(2\pi R)\sin(2\pi Z),\quad z(R,Z)=Z+0.1\sin(2\pi R)\sin(2\pi Z).$$

The vertices of the second mesh move stochastically. The range is centered at their previous locations yet confined in a square with the side length $h/4$. The shapes of these two meshes are shown in Fig. 7.

As regards the velocity fields in Fig. 8, field I is relatively smooth,

$$u=r-z+(r-1)^2-(z-1)^2,\quad v=r+z+(r-1)^2+(z-1)^2-2.$$

Conversely, field II contains obvious rise-and-fall,

$$u=\frac{\exp(20r-20)}{1+\exp(20r-20)},\quad v=0,$$

which can approximate the structure of a 1D shock.

The $\mathcal{L}_\infty$ errors of the vertex velocities calculated by three least-squares methods are listed in Fig. 9. Not only that, we assess their convergence rates using the meshes with various numbers of cells.

It is observed that these methods can reach the second-order convergence on "smooth" meshes, even when computing the more fluctuant field II. Simultaneously, it

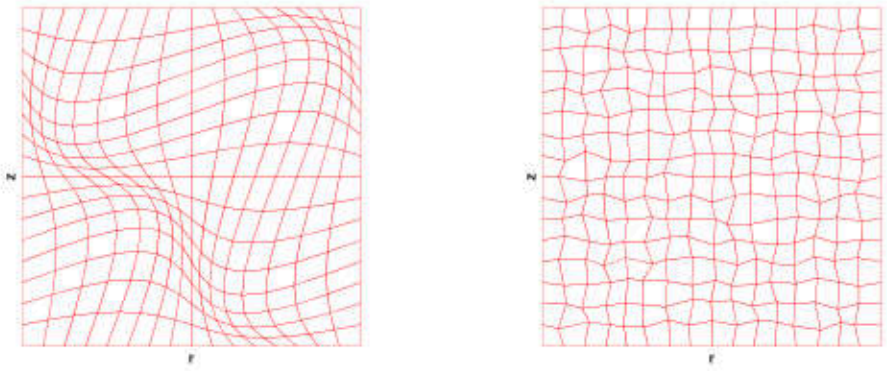

Fig. 7: The general shapes of two test meshes. Left: "smooth", right: random, $N=16$.

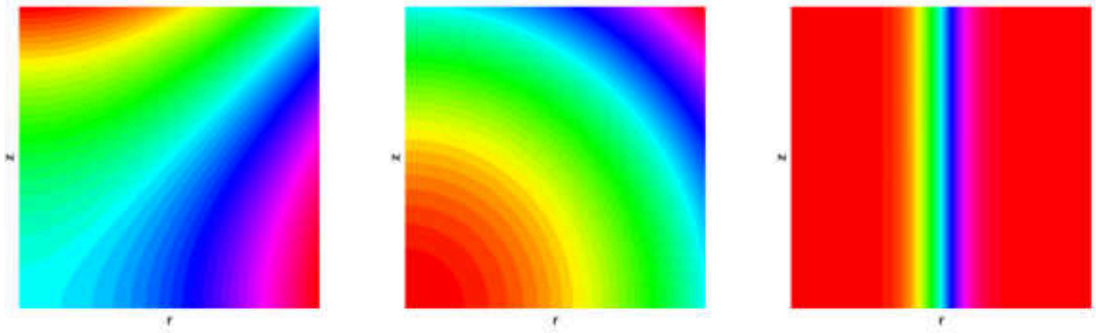

Fig. 8: The contour maps of two test velocity fields. Left: field I — u, middle: field I — v, right: field II — u.

should not be ignored that all of them experience convergence loss on random meshes. The five-point method even degenerates below first-order.

By overall comparison, our nine-point method attains minimal errors and basically sustains at second-order on the four cross combinations of distinct meshes and fields.

By pairwise comparison, the convergence rate of our method is much less correlated with the smoothness of meshes and velocity fields than the five-point version (Figs. 9(b) and 9(d)). Real Lagrangian meshes are full of uncertainties. They can be extraordinarily "discontinuous". Nevertheless, the five-point method has merits on robustness due to its simple stencil, see the leftmost subfigure of Fig. 6. Ours wins narrowly in Fig. 9(c).

Compared with the thirteen-point version, our method tightens the stencil and lowers the computational costs. As presented in Figs. 9(c) and 9(d), it captures the shock more precisely. Withal, we think that the selection of mid-points helps eliminate the redundant information and restore the flow direction. Numerical dissipation can thence be restrained (specially in Fig. 9(c)).

As far as the existing results are concerned, our nine-point least-squares method integrates advantages of the other two. It exhibits certain flexibility, acceptable robustness, and high-order accuracy.

6.2 The free expansion problem

We proceed to the next stage to test the accuracy of the GRP algorithm via the free expansion problem [10,20,22]. The material is initially static with the dimensionless values $\rho=1$ and $p=1-|\boldsymbol{x}|^2$ for $|\boldsymbol{x}|\leqslant 1$. The adiabatic index γ in (2.4) is set to $5/3$. The problem has the following analytical solution,

$$[\rho,|\boldsymbol{u}|,p]=\left[\frac{1}{R^3},\frac{2|\boldsymbol{x}|t}{1+2t^2},\frac{1}{R^5}\left(1-\frac{|\boldsymbol{x}|^2}{R^2}\right)\right],\quad \text{for } R(t)=\sqrt{1+2t^2}.$$

We list the numerical errors and the relevant convergence rates at $T=0.4$ in Table 1. To mitigate the influence of the peripheral area, the indicators are measured within the

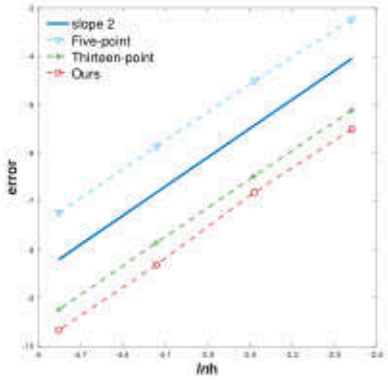

(a) Field I on "smooth" mesh.

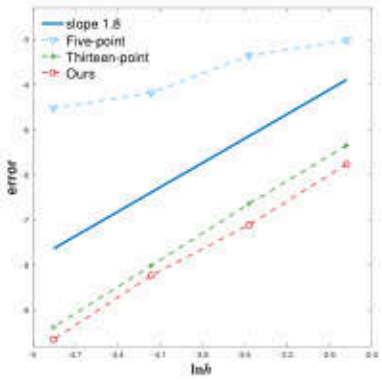

(b) Field I on random mesh.

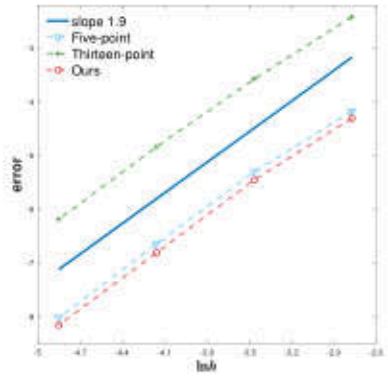

(c) Field II on "smooth" mesh.

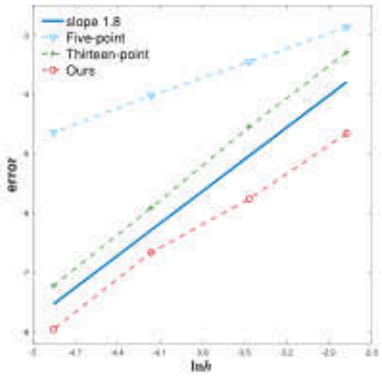

(d) Field II on random mesh.

Fig. 9: The $\mathcal{L}_\infty$ errors of the computed vertex velocities (sequentially make $N=16,32,64,128$). Solid line: a certain slope for comparison, triangle: result under five-point least-squares method, plus: result under thirteen-point method, circle: result under our nine-point method. The horizontal and vertical axes are in logarithmic scales.

interval $\boldsymbol{x}=(r,z)\in[0,0.9]\times[0,0.9]$. Evidently, our algorithm can attain the anticipated second-order accuracy in both $\mathcal{L}_\infty$ and $\mathcal{L}_1$ norms for all the evolved conserved variables.

6.3 The cylindrical and spherical Noh problems

Now we are eager to attempt the unique Noh problem [24] to validate our algorithm. It involves a radially symmetric converging flow of cold helium ($\gamma=5/3$). Its cylindrical scenario can be seen as a reduced-dimensional version of axisymmetric flows, with the

Table 1: The $\mathcal{L}_\infty$ and $\mathcal{L}_1$ errors of our algorithm for the free expansion problem.

N	Norm	Density	Order	Momentum	Order	Energy	Order
20	$\mathcal{L}_\infty$	3.91e-3		7.13e-3		1.02e-2	
	$\mathcal{L}_1$	5.15e-2		9.34e-2		9.16e-2	
40	$\mathcal{L}_\infty$	4.58e-4	3.09	8.61e-4	3.04	2.27e-3	2.16
	$\mathcal{L}_1$	8.77e-3	2.55	1.67e-2	2.48	2.37e-2	1.95
80	$\mathcal{L}_\infty$	7.44e-5	2.63	1.45e-4	2.57	4.87e-4	2.22
	$\mathcal{L}_1$	1.31e-3	2.74	3.66e-3	2.19	6.19e-3	1.93
160	$\mathcal{L}_\infty$	1.73e-5	2.11	3.85e-5	1.92	1.10e-4	2.14
	$\mathcal{L}_1$	3.62e-4	1.86	8.26e-4	2.15	1.98e-3	1.65

position vector $\boldsymbol{x}=(r,0)$. We distinguish it from the spherical one by setting $d=2$ for the former and $d=3$ for the latter. The initial conditions are $\rho=1$, $\boldsymbol{u}=-\boldsymbol{x}/|\boldsymbol{x}|$, and $p=0$.

According to the self-similar solution investigated in [13], a gradually enlarging shock sets off at the speed of $(\gamma-1)/2$ from the very start. The field behind it is stationary. And the "uniqueness" mostly lies in its rear constant density and pressure. Specifically, their pre-shock values are $\rho=(1+t/|\boldsymbol{x}|)^{d-1}$ and $p=0$, while the post-shock values are $\rho=[(\gamma+1)/(\gamma-1)]^d$ and $p=(\gamma+1)^d/2(\gamma-1)^{d-1}$.

In the cylindrical case, we layout 200×10 computational cells in the primal domain $[0,1]\times[0,1]$. It is compressed to $[0,0.4]\times[0,1]$ at T=0.6. The mesh variations and numerical results versus the r-axis are presented in Figs. 10 and 11.

Broadly speaking, each result resolves the shock sharply. They all match with the analytical solution in the pressure aspect, see Fig. 11(b). Our result (indicated as "circle") takes no remarkable superiority. However in the density aspect, it is much closer to the uniform value near $r=0$ than the others (Fig. 11(a)).

Overheating inevitably occurs in computing the Noh implosion. It is hard to be completely suppressed. The internal energy result under reflective boundary condition (indicated as "plus") is visibly too high to be portrayed, see Fig. 11(c). By contrast, our method is a top performer among these options. It is also comparable to those of [7, 20, 22]. Presumably, the one-sided GRP solver plays a role within.

The sort of spherical symmetric problems was nicely resolved on the polar meshes with equiangular zoning [10, 20, 30], since the arrangement of cells thereof could be aligned with the flow direction all along. We hope that our algorithm can also pull it off on the solely quadrilateral meshes.

The corresponding numerical results are presented in Fig. 12. Strong discontinuities and singularities at the symmetric r- and z-axes pose challenges to the calculations of fluxes, sources, and mesh motion. Nevertheless, our algorithm still exhibits the ability to preserve radial symmetry and ensures an admissible solution in such a severe test. The results become significantly better with the mesh refinement (Figs. 12(c) and 12(d)).

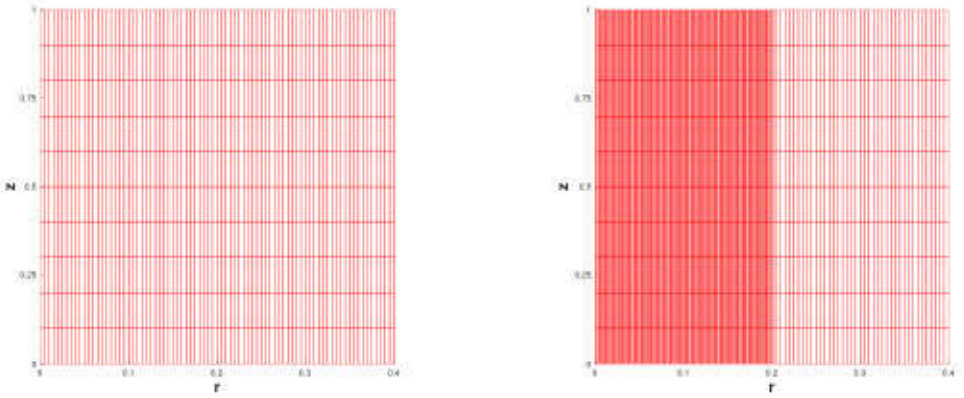

(a) Local initial one. (b) At $T=0.6$.

Fig. 10: The computational meshes of the cylindrical Noh problem at different times.

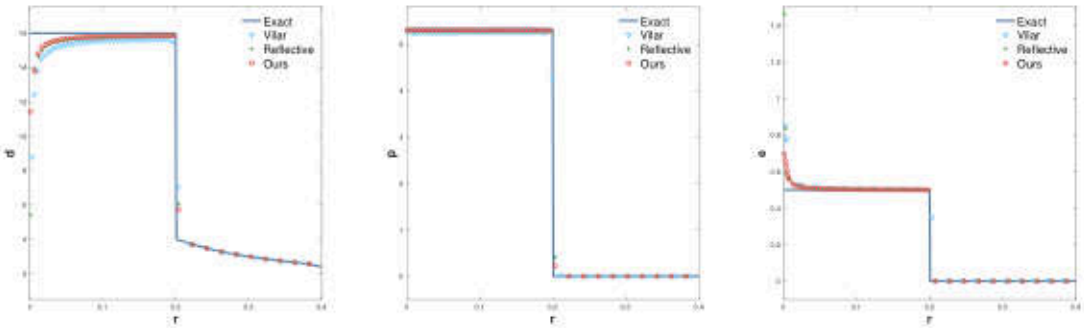

(a) Density. (b) Pressure. (c) Internal energy.

Fig. 11: The scatter plots of the cylindrical Noh problem at $T=0.6$. Solid line: analytical solution [13], triangle: Vilar's result [34], plus: result under reflective boundary condition, circle: our result.

Meanwhile, we must admit that it is difficult to obtain finer results at $T=0.6$ in pure Lagrangian simulations. That is partly because the least-squares method proposed in Section 4.1 is not completely precise. The numerical dissipation effects can mask the errors it generates. Yet when the mesh is refined somewhat, the errors may accumulate, amplify, and lead to spurious mesh deformations. The initial misalignment between the mesh and the flow is responsible for some negative consequences likewise.

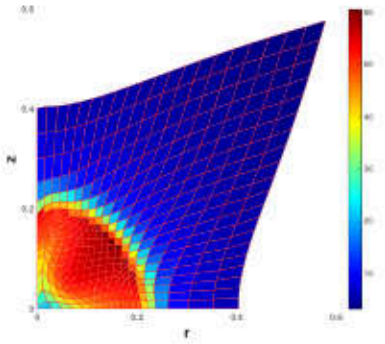

(a) Density distribution.

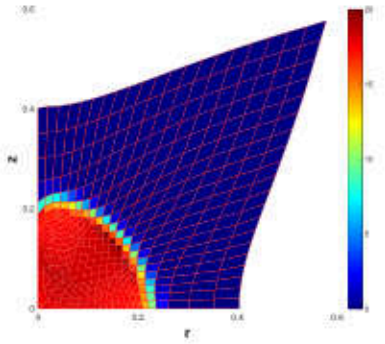

(b) Pressure distribution.

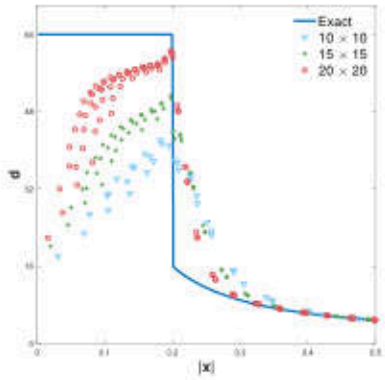

(c) Density scatters.

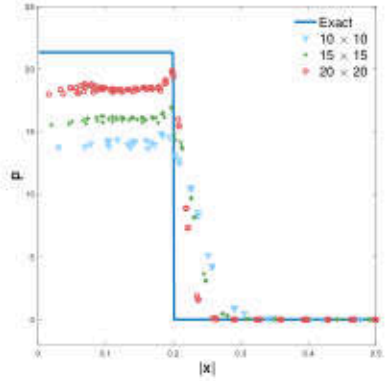

(d) Pressure scatters.

Fig. 12: The numerical results of the spherical Noh problem at $T=0.6$. Solid line: analytical solution [13]. The shape of a symbol changes with the number of cells in the mesh, triangle: 10×10, plus: 15×15, circle: 20×20.

6.4 Spherical 123 problem

The spherical 123 problem is selected to testify the validity of our method in simulating rarefaction propagation. The computational domain is $[0,4]\times[0,4]$ at the outset, wherein the density $\rho=1$ and the pressure $p=0.4$. The velocity is spherically outward of magnitude 2, $\gamma=1.4$.

Given the spherical symmetry, we can construct another one-sided GRP solver based on the boundary data $v(r,z=0,t)\equiv0$ and utilize it at the axis $z=0$ in our algorithm.

The expanding and increasingly rounded mesh with 50×50 cells is displayed in

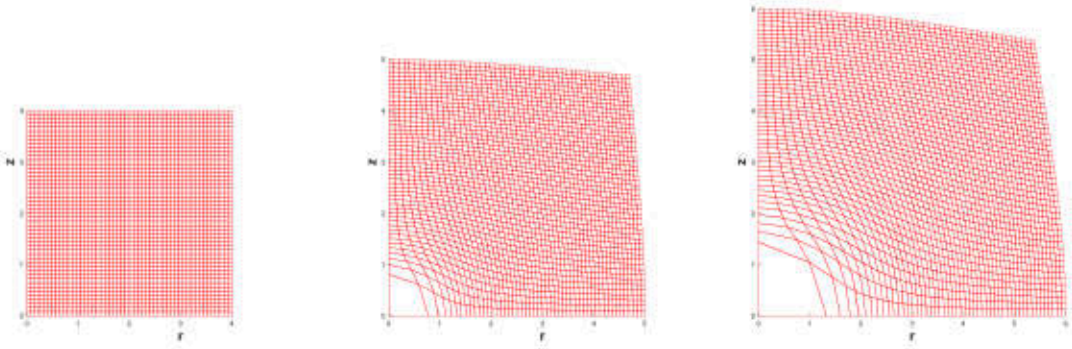

(a) Initial one. (b) At $T=0.5$. (c) At $T=1$.

Fig. 13: The computational meshes of the spherical 123 problem at different times.

Fig. 13. We sketch the simulation results at $T=1$ in Fig. 14. Therein the refined numerical solution got by a 1D code [19] is employed as a reference (labelled with "**Referential**"). The control group continues to use the reflective boundary condition at $z=0$.

In general, our result manifests preferable spherical symmetry, see Figs. 14(a)-14(c). As drawn in Figs. 14(d) and 14(e), all of the density and pressure values are in desirable agreement with the referential ones. Ours is optimal since the discrepancies are barely noticeable. Whereas these results behave differently in calculating the internal energy (Fig. 14(f)). In terms of the inhibition of overheating, ours occupies the first place. We attribute it to the contribution of the one-sided GRP solvers. Compared with the other treatments, they can describe the flows at the symmetric axes more precisely. This shall yield a positive consequence on calculating the cell averages nearby.

Additionally, we note that a flaw, the numerical oscillations near $|\boldsymbol{x}|=2$, appears in our internal energy result (Fig. 14(c)). We guess that there are two possible reasons. Firstly, the region right here is close to vacuum. From (2.4) we know that a tiny error of low-density or low-pressure may lead to a sizable deviation of internal energy. Secondly, compared with the one-sided GRP solver in Section 3.2, the newly imposed solver at the axis $z=0$ is actually built on dropping two disparate terms of the system (2.5), i.e. $\boldsymbol{G}(\boldsymbol{V})\partial\boldsymbol{V}/\partial r$ and $\boldsymbol{\Psi}(r,\boldsymbol{V})$. This may bring about the defects in the simulation of intense symmetric waves and deserve further discussion.

6.5 The Sedov–Taylor blast wave problem

The Sedov–Taylor problem is a classic test that has been widely used to confirm the capability of the Lagrangian algorithms in resolving the strong nonlinear waves [17,25].

The gas is initially still with $\rho=1$, $p=10^{-6}$, and $\gamma=1.4$. But the energy source at origin will immediately generate an outward traveling blast. The pressure inside the cell over

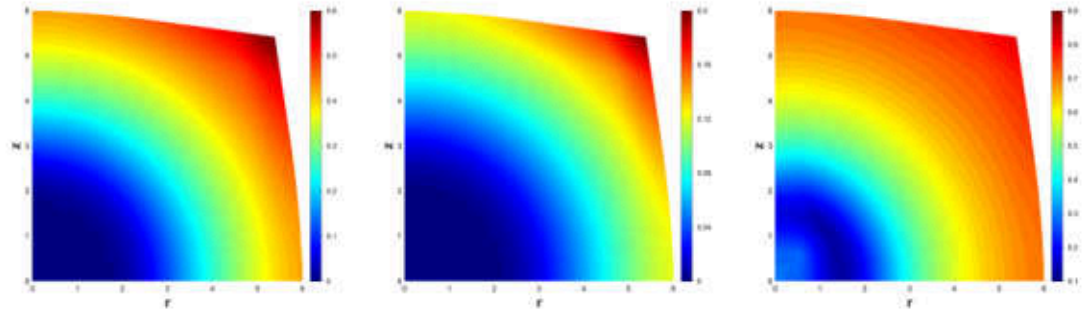

(a) Density contours. (b) Pressure contours. (c) Internal energy contours.

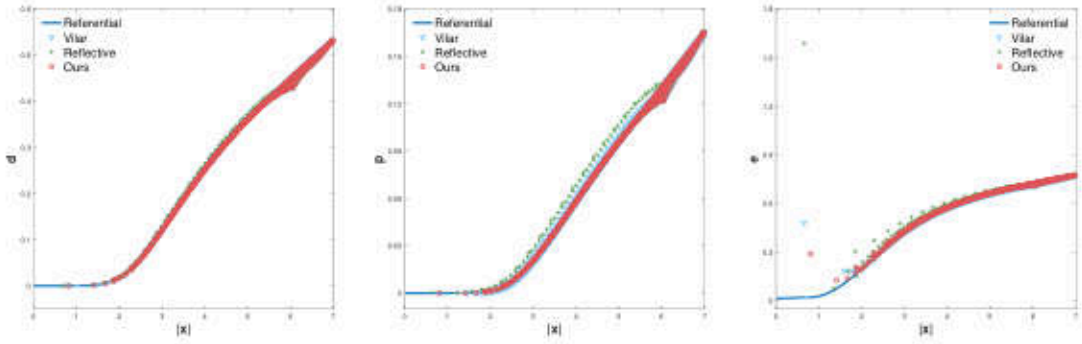

(d) Density comparison. (e) Pressure comparison. (f) Internal energy comparison.

Fig. 14: The numerical results of the spherical 123 problem at $T=1$ with 50 isolines in each contour map. Solid line: a refined Eulerian result [19], triangle: Vilar's method [33,34], plus: result under reflective boundary condition, circle: our result, the same hereinafter.

here is $p_0=(\gamma-1)\rho e_0/V_0$ with the cell volume V_0 and the total amount of released energy e_0. If we take $e_0=0.425536$, the shock front will be seated at $|\boldsymbol{x}|=1$ when $T=1$.

As plotted in Fig. 15, we demonstrate the meshes computed by three least-squares methods. There 30×30 square cells are initially laid in the zone $[0,1.2]\times[0,1.2]$. The shock of our nine-point method is closest to a spherical surface with the radius of 1 in contrast.

We discover that unlike Section 6.4, these meshes all put up more or less asymmetry (particularly the one in Fig. 15(a)). This may stem from the high pressure ratio in the problem setting. It makes the source term more crucial in determining the interface normal velocities. Thus the mesh motion differs markedly in the r and z axes. However, our result achieves a more satisfying effect due to the higher accuracy of the nine-point method. It leads the mesh to deform in the most likely orientation.

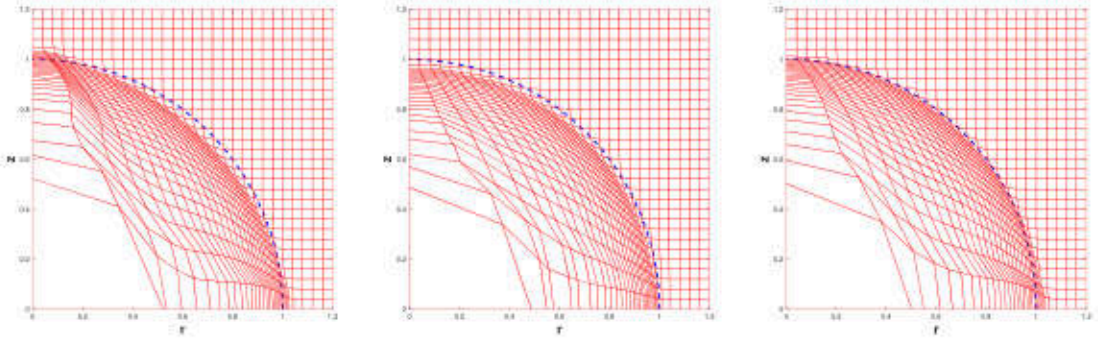

(a) Five-point. (b) Thirteen-point. (c) Our nine-point.

Fig. 15: The meshes of the Sedov–Taylor problem using different vertex least-squares methods at $T=1$. Dashed line: a quadrant for comparison.

The full and single views of the numerical results are given in Fig. 16. At a glimpse, we can make an intuitive judgment that the spherical symmetry is quite well preserved, see Figs. 16(a) and 16(b). To be clear, the isolines are kinda out of round behind the shock. It is probably because the quantities there varies greatly, while the mesh is sparse and shapes like a fishing net. So the graphics software fails to rebuild a completely circular distribution.

Our results look reasonable except for the negligible oscillations of two-story cells behind the shock (Figs. 16(c) and 16(d)). After careful inspection, we find that these cells are the ones closest to the axis $z=0$, i.e. $\Omega_{i,0}$ and $\Omega_{i,1}$ ($i\in\mathbb{N}^*$). A possible reason is what we have discussed in Section 6.4, the limitation of the one-sided GRP solver applied here. Even so, it still yields a finer performance than the reflective boundary condition. Concerning the latter, the shock waves are just like the mountain tops staggered from each other, some of which are incorrectly located. The same sort of phenomena also crops up in [9]. It tells us that the inappropriate numerical treatment at the symmetric axes might seriously backfire on the interior calculations.

Based on the analysis above, we can perceive that the resolution of vertex velocities and the choice of numerical boundary conditions can influence the outcome. Both of them are appreciated in our algorithm.

6.6 The bubble explosion

Now we are ready to take on the multi-material problem. Consider that a helium bubble ($\gamma=5/3$), centered at the position $\boldsymbol{x}_h=(0,6)$, stays in an air cylinder ($\gamma=1.4$) [21]. The

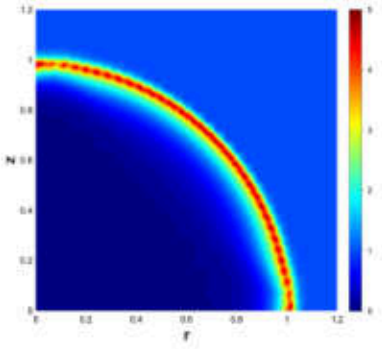

(a) Density contours.

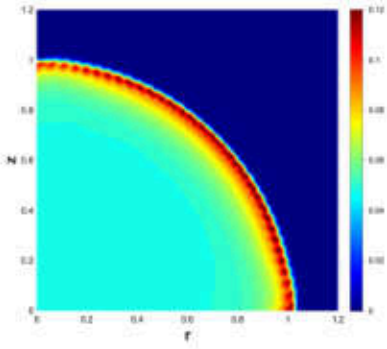

(b) Pressure contours.

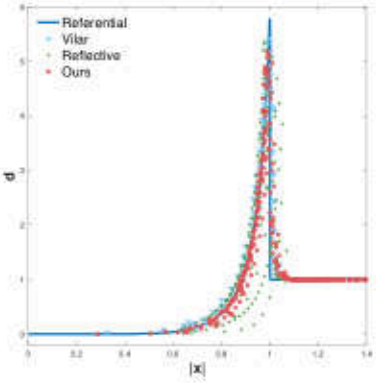

(c) Density comparison.

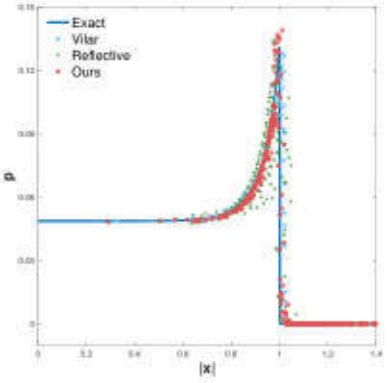

(d) Pressure comparison.

Fig. 16: The numerical results of the Sedov–Taylor problem at $T=1$.

bubble contains comparatively higher density and pressure,

$$[\rho,u,v,p]=\begin{cases}[2.25,0,0,18.3], & r^2+(z-6)^2<1,\\ [1,0,0,1], & \text{otherwise.}\end{cases}$$

The computational domain $[0,6]\times[0,12]$ is occupied by 60×120 cells. The mesh variation and density contours at four different moments $T=0.5$, 1, 1.5, and 2.19 are revealed in Fig. 17. The color bar on its lower right indicates the density level.

At $T=0.5$, an emerging shock propagates outwards. It causes an evident tightening of the external mesh around the material interface. Observed from the inside, the density value rapidly falls off and the mesh becomes looser because a strong rarefaction wave travels inwards at the same time, see Fig. 17(a).

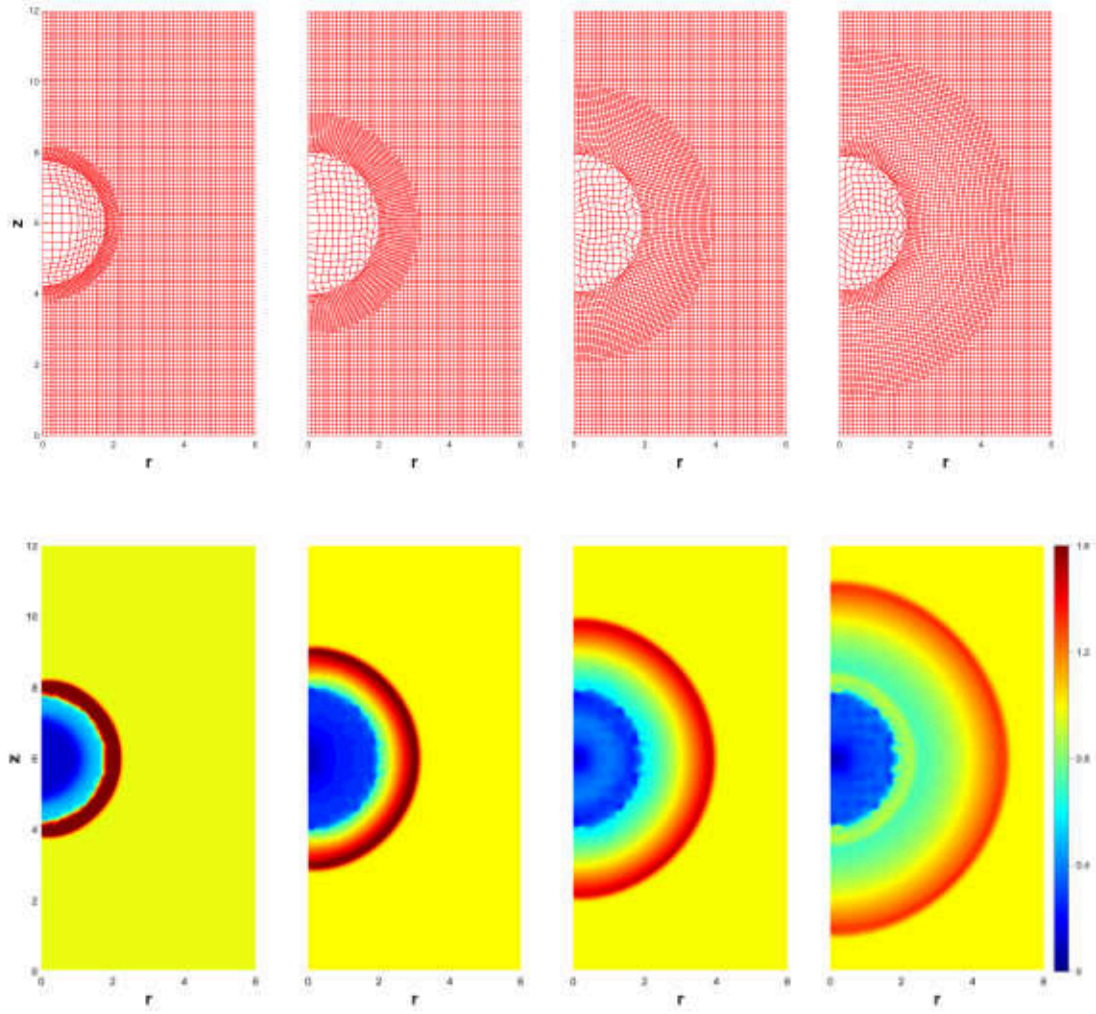

(a) $T=0.5$. (b) $T=1$. (c) $T=1.5$. (d) $T=2.19$.

Fig. 17: The numerical results of the bubble explosion at different times. The upper row: mesh variation, the bottom row: density contours.

At $T=1$, the expanding rate of the bubble appears to be slowing down, while the shock moves obviously faster. It almost arrives at the position $|\boldsymbol{x}-\boldsymbol{x}_h|=3$ (Fig. 17(b)).

At $T=1.5$, we can discern that a reflected shock has been generated from the collision between the rarefaction and the axis $r=0$. It remains trapped in the bubble. As drawn in Fig. 17(c), the ensuing changes are a marginal increase in density and a slight reduction in bubble size.

At $T=2.19$, the reflected shock has contacted with the material interface. The mesh

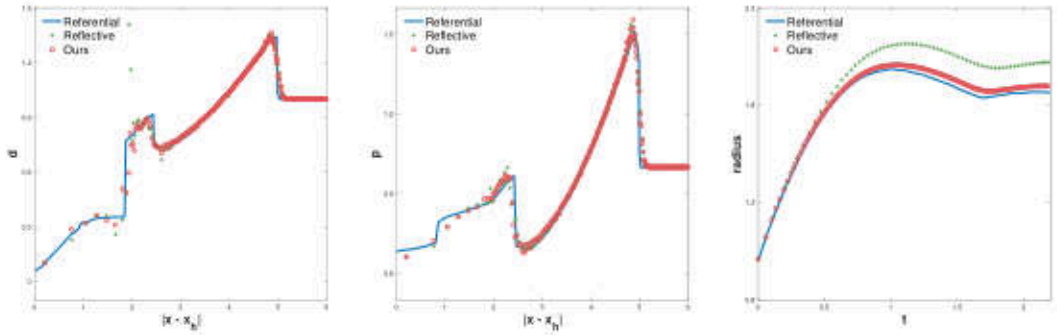

(a) Density at $T=2.19$. (b) Pressure at $T=2.19$. (c) Time-varying radius.

Fig. 18: The scatter plots of the bubble explosion. Solid line: referential result [35].

clinging to it shrinks again, see Fig. 17(d). The fluid takes on a complicated situation. Therefore, we present the density and pressure values along the distance from the bubble center $\boldsymbol{x}_h$ in Figs. 18(a) and 18(b). It can be perceived that an outward shock and a weaker inward one have been created. The former reaches the position around $|\boldsymbol{x}-\boldsymbol{x}_h|=2.4$, yet it is still far away from the first shock front (located near $|\boldsymbol{x}-\boldsymbol{x}_h|=5$).

Since the bubble repeatedly expands and contracts, we record its time-varying radius in Fig. 18(c). Compared with the result under reflective boundary condition, ours agrees better with the referential one. Overall, these three share a similar changing trend, yet suddenly diverge after $T=0.5$ when the rarefaction wave is getting close to $r=0$. The reflective boundary condition ignores the source effect. We analyze that it may result in an underestimation of kinetic energy and an overestimation of internal energy. The bubble is consequently bigger than the others. By contrast, our numerical boundary condition (2.12) is indeed derived from the governing equations (2.2) and takes such effect into account.

Reviewing the evolution of the fluid in Fig. 17, the first shock keeps a perfectly spherical shape. Well, it is not the case with the material interface. The geometrical errors of initial mesh partition and progressively concave cells, as well as the truncation errors of our scheme and least-squares resolution, can all be responsible for the few oscillations in density contours. Moreover, the Richtmyer–Meshkov and Rayleigh–Taylor instabilities can amplify them over time [8]. The higher-order development may contribute to mitigating the situation [11, 15].

7 Conclusion

In this study, a cell-centered Lagrangian algorithm is contrived for axisymmetric fluids. We prefer to use the same formulation of numerical boundary condition and the scheme

on interior cells, then realize it by geometrically compatible analysis on the control volume. Amidst the construction of numerical fluxes and sources, the required interface values are uniformly obtained by the GRP solver and its one-sided variant. In addition, we specifically design the next two important constitutes of the algorithm: the least-squares calculation of vertex velocities and the accordance with the GCL. The reliability of our handling is confirmed through various numerical experiments. Compared with the reflective boundary condition, the heating errors at the symmetric axis are suppressed to a certain extent.

A range of research can be developed on our algorithm: (i) Create its higher-order version to preserve interface symmetry. (ii) Extend it on arbitrary polygonal and curvilinear meshes to accommodate assorted requirements. (iii) Adjust it in actual scenarios to exert greater application value, such as the under-water explosion, bullet-shooting, and sliding detonation problems.

Acknowledgments

This work is partially supported by China Postdoctoral Science Foundation with No. GZC20231997, 2024M752451, Science Challenge Project with No. TZ2016002, National Key R & D Program of China 2022YFA1004500, 2023YFA1009002, NSFC with No. 11671050, 11771055, 12026607, 12102052, 12171049, 12171376, 12292982.

A The coefficients in the axisymmetric GRP solver

As pointed out in Section 3.1, the hinge of our axisymmetric GRP solver lies in the coefficients a_J, b_J, and d_J ($J=L$ or R) of the linear relations (3.14). For the readers' convenience, their values under different wave types are enumerated here. An extra superscript ("**rare**", "**shock**", or "**acous**") is added so that we can distinguish between the scenarios of rarefaction, shock, and acoustic wave. The newly added τ_0 means the position where the interface initially placed, scilicet $r^n_{i\pm1/2,j}$ or $r^n_{i,j\pm1/2}$ ($i\in\mathbb{N}^*$, $j\in\mathbb{Z}$).

A.1 Rarefaction wave

$$a_J^{\text{rare}}=1,\quad b_J^{\text{rare}}=-\frac{\text{sgn}(J)}{\rho_{J*}c_{J*}},$$

$$d_J^{\text{rare}}=\left(\frac{1+\mu^2}{1+2\mu^2}\vartheta_J^{\frac{1}{2\mu^2}}+\frac{\mu^2}{1+2\mu^2}\vartheta_J^{\frac{1+\mu^2}{\mu^2}}\right)T_J(S_{\tilde{\zeta}})_J+\text{sgn}(J)c_J\left(\chi'_J+\frac{n_r}{2\tau_0}\widetilde{u}_J\right)\vartheta_J^{\frac{1}{2\mu^2}}$$
$$+\frac{n_r}{2\tau_0}c_{J*}\left[\Upsilon_J+\text{sgn}(J)\widetilde{u}_*\right],$$

where the value Y_J is intimately connected with the adiabatic exponent γ,

$$\mathrm{Y}_J=\begin{cases}\dfrac{(\mu^2-1)c_{J*}}{\mu^2(4\mu^2-1)}\left(1-\vartheta_J^{\frac{1-4\mu^2}{2\mu^2}}\right)-\dfrac{\mathrm{sgn}(J)\chi_J}{2\mu^2-1}\left(1-\vartheta_J^{\frac{1-2\mu^2}{2\mu^2}}\right), & \text{if } \gamma\neq\dfrac{5}{3},\ \gamma\neq 3,\\ c_J-c_{J*}-\mathrm{sgn}(J)\chi_J\ln\vartheta_J, & \text{if } \gamma=3,\\ -2\cdot\left[3c_{J*}\ln\vartheta_J-\mathrm{sgn}(J)\chi_J(1-\vartheta_J)\right], & \text{if } \gamma=\dfrac{5}{3}.\end{cases}$$

Furthermore, T, S, and χ signify the temperature, the entropy, and the Riemann invariant,

$$\mu=\sqrt{\frac{\gamma-1}{\gamma+1}},\quad \vartheta_J=\frac{c_{J*}}{c_J},\quad T_J(S_\xi)_J=\frac{(p_\xi)_J-c_J^2(\rho_\xi)_J}{(\gamma-1)\rho_J},\quad \mathrm{sgn}(J)=\begin{cases}-1, \text{ if } J=L,\\ 1, \text{ if } J=R,\end{cases}$$

$$\chi_J=\begin{cases}\widetilde{u}_L+\dfrac{2c_L}{\gamma-1}, \text{ if } J=L,\\ \widetilde{u}_R-\dfrac{2c_R}{\gamma-1}, \text{ if } J=R,\end{cases}\quad \chi_J'=\begin{cases}(\widetilde{u}_\xi)_L+\dfrac{\gamma(p_\xi)_L-c_L^2(\rho_\xi)_L}{(\gamma-1)\rho_L c_L}, \text{ if } J=L,\\ (\widetilde{u}_\xi)_R-\dfrac{\gamma(p_\xi)_R-c_R^2(\rho_\xi)_R}{(\gamma-1)\rho_R c_R}, \text{ if } J=R.\end{cases}$$

A.2 Shock

$$a_J^{\text{shock}}=1+\mathrm{sgn}(J)\rho_{J*}(\sigma_J-\widetilde{u}_*)H_1^J,\quad b_J^{\text{shock}}=-\frac{\sigma_J-\widetilde{u}_*}{\rho_{J*}c_{J*}^2}-\mathrm{sgn}(J)H_1^J,$$
$$d_J^{\text{shock}}=L_\rho^J(\rho_\xi)_J+L_u^J(\widetilde{u}_\xi)_J+L_p^J(p_\xi)_J-\frac{n_r}{\tau_0}L_s^J,$$

where

$$\sigma_J=\frac{\rho_{J*}\widetilde{u}_*-\rho_J\widetilde{u}_J}{\rho_{J*}-\rho_J},\qquad L_\rho^J=\mathrm{sgn}(J)(\sigma_J-\widetilde{u}_J)H_3^J,$$
$$L_u^J=\sigma_J-\widetilde{u}_J-\mathrm{sgn}(J)\rho_J(c_J^2H_2^J+H_3^J),\qquad L_p^J=-\frac{1}{\rho_J}+\mathrm{sgn}(J)(\sigma_J-\widetilde{u}_J)H_2^J,$$
$$L_s^J=\mathrm{sgn}(J)\rho_J\widetilde{u}_J(c_J^2H_2^J+H_3^J)-(\sigma_J-\widetilde{u}_*)\widetilde{u}_*,$$

and the parameters $H_i^J=H_i(p_*;p_J,\rho_J)$ $(i=1,2,3)$ above are

$$H_1^J=\frac{1}{2}\sqrt{\frac{1-\mu^2}{\rho_J(p_*+\mu^2p_J)}}\cdot\frac{p_*+(1+2\mu^2)p_J}{p_*+\mu^2p_J},$$
$$H_2^J=-\frac{1}{2}\sqrt{\frac{1-\mu^2}{\rho_J(p_*+\mu^2p_J)}}\cdot\frac{(2+\mu^2)p_*+\mu^2p_J}{p_*+\mu^2p_J},\quad H_3^J=-\sqrt{\frac{1-\mu^2}{\rho_J(p_*+\mu^2p_J)}}\cdot\frac{p_*-p_J}{2p_J}.$$

A.3 Acoustic wave

$$a_J^{\text{acous}}=1,\quad b_J^{\text{acous}}=-\frac{\text{sgn}(J)}{\rho_J c_J},\quad d_J^{\text{acous}}=-\frac{(p_\xi)_J}{\rho_J}+\text{sgn}(J)\left[c_J(\widetilde{u}_\xi)_J+\frac{n_r}{\tau_0}c_J\widetilde{u}_J\right].$$

References

[1] F. L. Adessio, J. R. Baumgardner, J. K. Dukowicz, N. L. Johnson, R. M. Rauenzahn, and C. Zemach. CAVEAT: A computer code for fluid dynamics problems with large distortion and internal slip. Los Alamos National Laboratory Technical Report, LA-10613-MS, 1992.

[2] T. J. Barth and D. C. Jespersen. The design and application of upwind schemes on unstructured meshes. AIAA 27th Aerospace Sciences Meeting, 89-0366:1–12, 1989.

[3] M. Ben-Artzi and J. Falcovitz. A second-order Godunov-type scheme for compressible fluid dynamics. Journal of Computational Physics, 55(1):1–32, 1984.

[4] M. Ben-Artzi and J. Falcovitz. Generalized Riemann Problems in Computational Fluid Dynamics. Cambridge University Press, Cambridge, 1st edition, 2003.

[5] M. Ben-Artzi and J. Li. Hyperbolic balance laws: Riemann invariants and the generalized Riemann problem. Numerische Mathematik, 106(3):369–425, 2007.

[6] M. Ben-Artzi, J. Li, and G. Warnecke. A direct Eulerian GRP scheme for compressible fluid flows. Journal of Computational Physics, 218(1):19–43, 2006.

[7] W. Boscheri, D. S. Balsara, and M. Dumbser. Lagrangian ADER-WENO finite volume schemes on unstructured triangular meshes based on genuinely multidimensional HLL Riemann solvers. Journal of Computational Physics, 267:112–138, 2014.

[8] Y. Chen and S. Jiang. Various challenges in numerical simulation of three-dimensional multiphysics and multi-material problems under extreme conditions. Scientia Sinica Mathematica, 54(3):313–336, 2024.

[9] J. Cheng and C.-W. Shu. A high order ENO conservative Lagrangian type scheme for the compressible Euler equations. Journal of Computational Physics, 227(2):1567–1596, 2007.

[10] J. Cheng and C.-W. Shu. A cell-centered Lagrangian scheme with the preservation of symmetry and conservation properties for compressible fluid flows in two-dimensional cylindrical geometry. Journal of Computational Physics, 229:7191–7206, 2010.

[11] V. Dobrev, T. Kolev, and R. Rieben. High-order curvilinear finite element methods for Lagrangian hydrodynamics. SIAM Journal on Scientific Computing, 34(5):B606–B641, 2012.

[12] C. Feng, T. Liu, L. Xu, and C. Yu. Modified ghost fluid method with axisymmetric source correction (MGFM/ASC). Communications in Computational Physics, 28(2):621–660, 2020.

[13] P. Glaister. Flux difference splitting for the Euler equations with axial symmetry. Journal of Engineering Mathematics, 22(2):107–121, 1988.

[14] E. Han, J. Li, and H. Tang. Accuracy of the adaptive GRP scheme and the simulation of 2-D Riemann problems for compressible Euler equations. Communications in Computational Physics, 10(3):577–609, 2011.

[15] X. Ji, L. Pan, W. Shyy, and K. Xu. A compact fourth-order gas-kinetic scheme for the Euler and Navier–Stokes equations. Journal of Computational Physics, 372:446–472, 2018.

[16] S. Jin. A steady-state capturing method for hyperbolic systems with geometrical source terms. ESAIM Mathematical Modeling and Numerical Analysis, 35:631–645, 2001.

[17] J. R. Kamm and F. X. Timmes. On efficient generation of numerically robust Sedov solutions. Los Alamos National Laboratory Technical Report, LA-UR-07-2849, 2007.

[18] J. Li. Two-stage fourth order: Temporal-spatial coupling in computational fluid dynamics (CFD). Advances in Aerodynamics, 1(3):1–36, 2019.
[19] J. Li, T. Liu, and Z. Sun. Implementation of the GRP scheme for computing radially symmetric compressible fluid flows. Journal of Computational Physics, 228(1):5867–5887, 2009.
[20] D. Ling, J. Cheng, and C.-W. Shu. Positivity-preserving and symmetry-preserving Lagrangian schemes for compressible Euler equations in cylindrical coordinates. Computers & Fluids, 157:112–130, 2018.
[21] T. Liu, B. C. Khoo, and C. Wang. The ghost fluid method for compressible gas-water simulation. Journal of Computational Physics, 204(1):193–221, 2005.
[22] X. Liu, N. Morgan, and D. Burton. A comparative study of two different methods for RZ axisymmetric coordinates in context of Lagrangian discontinuous Galerkin hydrodynamics. AIAA Aviation and Aeronautics Forum and Exposition, LA-UR-18-24126:1–30, 2018.
[23] P. H. Maire. A high-order cell-centered Lagrangian scheme for compressible fluid flows in two-dimensional cylindrical geometry. Journal of Computational Physics, 228(18):6882–6915, 2009.
[24] W. F. Noh. Errors for calculations of strong shocks using an artificial viscosity and an artificial heat flux. Journal of Computational Physics, 72(1):78–120, 1987.
[25] C. Pederson, B. Brown, and N. Morgan. The Sedov blast wave as a radial piston verification test. Journal of Verification, Validation and Uncertainty Quantification, 1(3):031001, 2016.
[26] J. Qi, B. Tian, and J. Li. A high-resolution cell-centered Lagrangian method with a vorticity-based adaptive nodal solver for two-dimensional compressible Euler equations. Communications in Computational Physics, 24(3):774–790, 2018.
[27] J. Qi, Y. Wang, and J. Li. Remapping-free adaptive GRP method for multi-fluid flows I: One dimensional Euler equations. Communications in Computational Physics, 15(4):1029–1044, 2014.
[28] M. Shashkov and S. Steinberg. Conservative finite-difference methods on general grids. CRC Press, Boca Raton, 1st edition, 1996.
[29] M. Shashkov, B. Swartz, and B. Wendroff. Local reconstruction of a vector field from its normal components on the faces of grid cells. Journal of Computational Physics, 139(2):406–409, 1998.
[30] Z. Shen, X. Li, and J. Ren. Comparisons of some difference forms for compressible flow in cylindrical geometry on arbitrary Lagrangian and Eulerian framework. Applied Mathematics and Mechanics, 37(11):1–16, 2016.
[31] T. Tang, R. Li, and Z. Zhang. Moving Mesh Methods for Computational Fluid Dynamics. Science Press, Beijing, 1st edition, 2023.
[32] E. F. Toro. Riemann Solvers and Numerical Methods for Fluid Dynamics. Springer, Heidelberg, 3rd edition, 2009.
[33] F. Vilar, C.-W. Shu, and P. H. Maire. Positivity-preserving cell-centered lagrangian schemes for multi-material compressible flows: From first-order to high-orders. Part I: The one-dimensional case. Journal of Computational Physics, 312:385–415, 2016.
[34] F. Vilar, C.-W. Shu, and P. H. Maire. Positivity-preserving cell-centered Lagrangian schemes for multi-material compressible flows: From first-order to high-orders. Part II: The two-dimensional case. Journal of Computational Physics, 312:416–442, 2016.
[35] C. Wang, H. Tang, and T. Liu. An adaptive ghost fluid finite volume method for compressible gas-water simulations. Journal of Computational Physics, 227(12):6385–6409, 2008.
[36] K. Wu and H. Tang. A direct Eulerian GRP scheme for spherically symmetric general relativistic hydrodynamics. SIAM Journal on Scientific Computing, 38:B458–B489, 2016.

[37] J. Zhang, H. Han, and H. Brunner. Numerical blow-up of semilinear parabolic PDEs on unbounded domains in $\mathbb{R}^2$. Journal of Scientific Computing, 49(3):367–382, 2011.
[38] Z. Zhu, Q. Cui, and G. Ni. A high-resolution scheme for axisymmetric hydrodynamics based on the 2D GRP solvers. Computers & Fluids, 264:105961, 2023.
[39] Z. Zhu, X. Hu, and G. Ni. Radially symmetrical problems for compressible fluids with a high-resolution boundary condition. Advances in Applied Mathematics and Mechanics, 15(2):428–449, 2023.